H-930709-1

Optical Absorption in Fused Silica During Irradiation at High-Temperature

NASA Contract No. NASw-847

UNITED AIRCRAFT CORPORATION

United Aircraft Research Laboratories

EAST HARTFORD, CONNECTICUT

United Aircraft Research Laboratories

UNITED AIRCRAFT CORPORATION

EAST HARTFORD, CONNECTICUT

H-930709-1

Optical Absorption in Fused Silica

During Irradiation at High-Temperature

NASA Contract No. NASw-847

REPORTED BY Gary E. Palma
Gary E. Palma
Ronald M. Gagosz
Ronald M. Gagosz

APPROVED BY Robert K. Erf
Robert K. Erf, Chief
Optics and Acoustics

DATE November 1969

NO. OF PAGES 60

COPY NO. 65

FOREWORD

An exploratory experimental and theoretical investigation of gaseous nuclear rocket technology has been conducted by the United Aircraft Research Laboratories under Contract NASw-847 with the joint AEC-NASA Space Nuclear Propulsion Office. The Technical Supervisor of the Contract for NASA is Captain C. E. Franklin (USAF). Results of portions of the investigation conducted during the period between August 6, 1968 and November 15, 1969 relative to radiation damage to transparent materials is described in the present report, which comprises the required tenth Interim Summary Technical Report under the Contract.

Report H-930701-1

Optical Absorption in Fused Silica During Irradiation at High-Temperature

TABLE OF CONTENTS

Report H-930709-1

Optical Absorption in Fused Silica During Irradiation at High-Temperature

SUMMARY

In situ optical experiments were conducted to determine the level of irradiation-induced optical absorption that exists in Corning Grade 7940 fused silica at elevated temperatures during 1.5-Mev electron irradiation and during nuclear reactor irradiation. The optical absorption was measured at the peak of the strong irradiation-induced absorption band in fused silica centered at 2150 Å over a range of specimen temperatures from 170 to 900 C. Several additional measurements were made at longer wavelengths (2700 Å and 4500 Å) to investigate the width of the absorption band and to check the absorption where strong absorption bands are not expected to exist.

The electron irradiation experiments were conducted at the NASA Langley Research Center using a Dynamitron electron accelerator as a source of 1.5-Mev electrons. The accelerator provided current densities in the range 20 to 150 microamp/cm^2 corresponding to estimated ionizing dose rates of 2.7 to 20 x 10^6 R/sec deposited in the specimen. The induced absorption and specimen temperature were measured before, during, and after the irradiation; transient, as well as steady state, data were obtained. The nominal irradiation time for the electron irradiation experiments was 1000 sec.

The reactor irradiation experiments were conducted at the Air Force Institute of Technology using a 10 megw, swimming pool reactor as a source of fast neutrons and gamma rays. The fast neutron flux ($E > 0.75$ Mev) and ionizing dose rate at full power were 1.7 x $10^{12}/cm^2$-sec and 0.02 x 10^6 R/sec, respectively, at the location of the specimen. The induced absorption was measured during the irradiation at constant reactor power and specimen temperature in order to obtain equilibrium values. The nominal irradiation time for the reactor experiments was 3.5 x 10^5 sec.

RESULTS

1. Measurement of the optical transmission of fused silica during the electron irradiation experiments indicate that:

   a. no equilibrium irradiation-induced absorption occurred in the specimen at a wavelength of 2700 Å, an ionizing dose rate of 10.6×10^6 R/sec (80 microamp/cm^2), and a specimen temperature of 540 C;

   b. at a wavelength of 2150 Å, an ionizing dose rate of 2×10^7 R/sec (150 microamp/cm^2), and a specimen temperature of 900 C the measured equilibrium irradiation-induced absorption coefficient was 12 cm^{-1} and;

   c. at a wavelength of 2150 Å, over a range of specimen temperatures (170 to 900 C) and over a range of ionizing dose rates (2.7 to 20 x 10^6 R/sec), the equilibrium irradiation-induced absorption coefficient was an increasing function of ionizing dose rate and a decreasing function of specimen temperature. The induced absorption coefficients rose to an equilibrium value with time constants on the order of 100 sec, the exact value depending on the ionizing dose rate and the initial specimen temperature. The induced absorption coefficient decayed at the end of the irradiation with a time constant of several seconds, the exact value depending on the specimen temperature.

2. Measurement of the optical transmission of fused silica during the reactor irradiation experiments indicate that:

   a. at a wavelength of 2700 Å, an ionizing dose rate of 2×10^4 R/sec and a specimen temperature of 900 C, the measured equilibrium irradiation-induced absorption coefficient was 0.01 cm^{-1} and;

   b. at a wavelength of 2150 Å and a specimen temperature of 900 C, the measured equilibrium irradiation-induced absorption coefficient was 0.034 cm^{-1} at an ionizing dose rate of 2×10^4 R/sec and 0.015 cm^{-1} at an ionizing dose rate of 1×10^4 R/sec.

3. In the absence of optical bleaching, the results indicate that, in an operating nuclear light bulb engine, the equilibrium absorption at 900 C would be approximately 3.0 cm^{-1} based upon the electron irradiation experiments and approximately 8.3 cm^{-1} based upon the nuclear irradiation experiments.

4. Results from a single optical bleaching experiment indicate that optical bleaching in a nuclear light bulb engine may result in a significant decrease in equilibrium absorption.

INTRODUCTION

The Research Laboratories of United Aircraft Corporation are investigating various technologies associated with gaseous nuclear rocket engines under Contract NASw-847 with the joint AEC-NASA Space Nuclear Propulsion Office. One of the engine concepts to which these technologies can be applied is the nuclear light bulb concept, which is based on the transfer of energy by thermal radiation from gaseous nuclear fuel through an internally-cooled transparent wall to a seeded hydrogen propellant. The prime candidate material for the transparent wall at present is a high purity grade of fused silica, such as Corning Grade 7940, for reasons of structural integrity, ease of fabrication, good thermal properties, resistance to radiation damage, and transparency over a wide range of wavelengths.

During normal operation the transparent wall will be exposed to a large flux of fast neutrons and gamma rays which emanate from the fissioning fuel region as discussed in Ref. 1. The resulting ionization and damage can result in the generation of color centers in the wall material with a subsequent loss of transparency (Refs. 2 through 6). The center of the most prominent irradiation-induced absorption band in Corning Grade 7940 fused silica occurs at a wavelength of 2150 Å with a subsidiary peak occurring at approximately 2700 A. Since the color centers are unstable above room temperature, the irradiation-induced optical absorption can be minimized by maintaining the transparent wall at elevated temperatures (500 to 900 C).

Several experimental programs have been conducted in an attempt to determine the level of the irradiation-induced optical absorption which may be expected in the transparent wall of the nuclear light bulb (NLB) engine when the wall is maintained at elevated temperatures. In two of these programs, described in Refs. 7 and 8, measurements of the irradiation-induced absorption were obtained after reactor irradiations at elevated temperatures and subsequent gamma ray irradiations at room temperature. Additional measurements were made of the decay of the irradiation-induced absorption during post-irradiation elevated-temperature treatments. These experiments were useful in the determination of the rate of decay of the irradiation-induced absorption at elevated temperatures and in establishing the importance of gamma rays as a source of induced absorption. However, it was not obvious how measurements made after irradiation could be used to determine the level of absorption occurring during irradiation.

Consequently, a third experimental program was conducted in which the optical absorption of fused silica was measured at ambient and at elevated temperatures during irradiation by a pulse of fast neutrons and gamma rays from the University of Illinois' Triga Reactor, and is described in Refs. 9 and 10. This reactor pulse provided a fast neutron flux and ionizing dose rate, due to gamma rays, that was comparable to that expected in the full-scale engine, but for a period of time of 30 msec, which is considerably less than the nominal 1000 sec running time of the engine. In addition to demonstrating the feasibility of conducting in situ

irradiation experiments, transient data were obtained which indicated that, during the peak of the pulse, approximately 0.01 cm^{-1} of absorption is present at specimen temperatures of 900 C. However, equilibrium data could not be obtained in these experiments, limiting the applicability of these data in determining the absorption in the transparent wall of an operating full-scale engine.

The experimental program described in this report was conducted to obtain steady state, rather than transient, in situ measurements of irradiation-induced absorption in fused silica. These experiments consisted of measurements of the irradiation-induced absorption at elevated temperatures (as high as 900 C) during reactor irradiation and during irradiation by fast electrons from a linear electron accelerator. The latter experiment provided a simulation of the effects of the ionizing dose rate expected in the full-scale engine, while the former experiment provided a simulation of both ionizing radiation and neutrons, but at a flux that was about two orders of magnitude lower than that expected in the full-scale engine. The motivation, design, procedure, and results for each of these experiments are described in the following sections, and a discussion of the irradiation-induced absorption expected in the full-scale engine is given.

GENERAL DISCUSSION OF IRRADIATION-INDUCED OPTICAL ABSORPTION IN FUSED SILICA

Before proceeding to a discussion of the experiments, it is necessary to review the nature of the irradiation-induced optical absorption in fused silica. Fused silica can be obtained in a wide range of grades, from commercial grades of relatively low quality, to a number of grades of very high quality. The tests discussed in the following sections were conducted using specimens of Corning Grade 7940 fused silica, which is representative of a number of products of very high quality; in much of the following discussion the term "Corning Grade 7940 fused silica" represents any of these high-quality products. In most commercial grades of fused silica, exposure to neutrons and ionizing radiation generates a large number of optical absorption bands at visible and ultraviolet wavelengths. The majority of these irradiation-induced absorption bands are believed to be due to the presence of certain impurities in the fused silica. Corning Grade 7940 fused silica is essentially free of impurities except for a controlled amount of water ($\sim$ 0.1 percent). This grade of fused silica exhibits a single irradiation-induced absorption band centered at 2150 Å with a subsidiary peak sometimes occurring at slightly longer wavelengths (2500 to 2700 Å). Figure 1 is a plot of the relative transmission of Corning Grade 7940 fused silica before and after repeated gamma irradiations, from Ref. 8, which indicates the spectral nature of the irradiation-induced absorption band. The intrinsic ultraviolet absorption edge ($\sim$ 1600 Å) at which the fused silica becomes essentially opaque is also indicated in this figure. The growth of the absorption band at 2150 Å with increasing radiation dose is slower in Corning 7940 fused silica than in lower quality commercial grades of fused silica. This is believed to be due to quenching of the irradiation-induced absorption by the large water content, although the detailed quenching mechanism is not known. Since Corning Grade 7940 fused silica is more resistant to irradiation-induced optical absorption than lower quality commercial grades of fused silica, exclusive attention has been given to this grade of fused silica in the present experimental program.

The generation of the irradiation-induced absorption band at 2150 Å in fused silica is believed to be a two-step process that first requires the presence of a particular defect in the glass structure rather than a substitutional impurity. This defect is an oxygen vacancy which results in a positively charged $(SiO)^+$ ion that can act as a trap for electrons. These defects can be generated in several ways. An incident neutron can remove an oxygen ion from the SiO_2 molecule resulting in a positively charged $(SiO)^+$ ion which can be separated many atomic distances from the displaced oxygen ion, thereby creating a vacancy interstitial pair. The oxygen ion can acquire considerable kinetic energy in this type of collision and may produce a large number of additional defects in a cascade process. Ionizing radiation (gamma rays or fast electrons) can also generate these defects by rupturing the silicon-oxygen bond in the SiO_2 molecule, resulting in a negatively charged O^- ion which is not significantly displaced from the positive $(SiO)^+$ ion. In addition, a significant concentration of these defects may be present in the

absence of irradiation due to the intrinsic disorder in the glass structure.

Ordinarily, fused silica is a good insulator so that only a small number of free electrons are available for trapping at these defects. However, ionizing radiation generates a significant amount of free electrons which can then be trapped at the positively charged defects. The resulting complex, consisting of an electron trapped at a positively charged defect, is believed to be responsible for the irradiation-induced absorption band centered at 2150 Å in fused silica. In agreement with established usage, this complex is termed a color center, although, in this case the absorption is at an ultraviolet rather than a visible wavelength. The growth of the irradiation-induced absorption coefficient at 2150 Å with increasing ionizing dose is illustrated in Fig. 2. This curve was obtained by measuring the irradiation-induced absorption coefficient at the end of consecutive ambient-temperature gamma irradiations from a Co-60 source, as described in Ref. 8. The curve is a straight line with a slope of approximately 0.043 cm^{-1}/Mrad. The addition of neutron damage is expected to alter this curve somewhat due to the additional defects produced by the displacement effects mentioned previously. However, the results of the TRIGA experiments (Refs. 9 and 10) did not indicate any additional effects due to neutron damage, in that the induced absorption coefficient measured at ambient specimen temperature at the end of the radiation pulse was equal to that obtained by multiplying the slope of the gamma irradiation curve, 0.043 cm^{-1}/Mrad, by the ionizing dose of the pulse.

At ambient temperature the color centers responsible for the absorption band at 2150 Å are relatively stable. However, at elevated temperatures there are several processes that are effective in annihilating these color centers. First, the thermal vibrations in the neighborhood of the color center can liberate the trapped electron. This process is referred to as thermal bleaching and results in partial annihilation of the color center, since the defect is still present. Second, a recombination of the $(SiO)^+$ ion with an O^- ion can occur, resulting in complete annihilation of the color center. This process is referred to as thermal annealing. The effectiveness of these processes is indicated in Fig. 3 in which the measured time constant for the removal of reactor-induced absorption at 2150 Å is plotted against specimen temperature, as described in Ref. 8. The time constant varies from 500 sec at 300 C to 34 sec at 900 C. In addition to the thermal removal of coloration, absorption of light by the color center can result in liberation of the trapped electron. This is referred to as optical bleaching, and is a function of the intensity and spectral distribution of the bleaching light.

Differential equations whose solutions describe the variation of the concentration of color centers with time during irradiation have been derived and are presented in Appendix A. The solutions of these equations have been used in predicting the behavior of the induced absorption coefficient in each experiment and in the correlation and interpretation of the resulting data. Equations were derived corresponding to two distinct models of the coloration process. In the first model it is assumed that the defects responsible for the induced absorption are generated by the incident radiation and that the defects anneal at elevated temperatures. In the second model

it is assumed that the defects responsible for the coloration are present in the material in the absence of radiation due to intrinsic disorder in the glass structure and do not anneal at elevated temperatures. The actual coloration process in fused silica is probably best described by a combination of these two models, although it is not possible to determine which model is predominant with the available experimental data. Several approximations were made in the derivation of these equations. These include the neglect of the effects of neutron damage and the assumption that the generation, bleaching, and annealing of color centers are all first-order processes.

The resulting irradiation-induced absorption coefficient is directly proportional to the concentration of color centers and is given by:

$$\alpha(\lambda) = \sigma_{ph}(\lambda) N_c \qquad (1)$$

where:

$\alpha(\lambda)$ = induced absorption coefficient at the wavelength, λ, (cm^{-1})

$\sigma_{ph}(\lambda)$ = optical absorption cross section at the wavelength, λ, (cm^2)

N_c = concentration of color centers (cm^{-3})

The equilibrium values of the color center concentration predicted by the equations in Appendix A are of particular interest in that, when substituted into Eq. (1), they can be used to make quantitative comparisons of the results of the various experiments, and to estimate the level of irradiation-induced absorption expected in the transparent wall of the full-scale engine. The functional form of the equilibrium irradiation-induced absorption coefficient depends in general upon the particular model chosen. However, under the restrictions described in Appendix A, Eq. (1) in either case reduces to the following simple functional form,

$$\alpha = g\dot{D}\tau \qquad (2)$$

where:

α = equilibrium induced absorption coefficient (cm^{-1})

g = generation rate due to ionizing radiation (cm^{-1}/Mrad)

$\dot{D}$ = ionizing dose rate (Mrad/sec)

τ = time constant for thermal removal of coloration (sec)

The effect of optical bleaching on the magnitude of the equilibrium induced absorption coefficient is also discussed in Appendix A. The resulting decrease in the equilibrium

absorption coefficient due to an optical bleaching rate that is proportional to the light intensity is indicated in Fig. 4 for several values of the combined electron trapping and thermal decoloration rates. As can be seen in Fig. 4, optical bleaching can result in a significant decrease in the induced absorption if the decoloration rate due to optical bleaching is greater than the combined electron trapping and thermal decoloration rates.

ELECTRON IRRADIATION EXPERIMENTS

Measurements of the optical transmission of Corning Grade 7940 fused silica at elevated temperatures during electron irradiation were conducted at the Space Radiation Effects Laboratory of the NASA Langley Research Center, Hampton, Virginia. The experiments were conducted using the Dynamitron electron accelerator as a source of high energy (1.5 Mev) electrons to simulate the ionizing dose rate of an operating nuclear light bulb engine. The specimen was in the form of a thin (1.5-mm) wafer to minimize the effects of dielectric breakdown of the fused silica and large thermal gradients, and was mounted outside the accelerator beam port. With this configuration, a maximum current density of 150 microamperes/cm^2 (corresponding to an ionizing dose rate of 2×10^7 R/sec) could be provided through the titanium window on the beam port of the accelerator. The entire optical system was located in the immediate vicinity of the electron beam and hence was in a large radiation field. To minimize the effect of the scattered radiation on the measuring circuitry, a dual-optical-beam system and phase-sensitive-detection was used.

Electron Current Density

Transmittance measurements, during the irradiation, were obtained over a range of electron current densities (20 to 150 microamperes/cm^2) to determine the effects of the irradiating flux on the irradiation-induced optical absorption. To simplify the experimental apparatus, the specimen was mounted outside the vacuum system of the accelerator and a thin (0.001-in.) water cooled titanium window, mounted on the beam port of the accelerator, was used to transmit the electron beam from the vacuum to the atmosphere. The maximum electron beam current density allowed through the titanium window to minimize the possibility of rupture is 150 microamperes/cm^2. The end window, in addition, causes scattering of the electron beam which results in loss of collimation of the beam upon transmission. An additional aperture between the end window of the accelerator and the specimen was used to reduce the scattering and maintain a beam size of approximately 1 cm^2 at the specimen, which is located 0.75-in. from the aperture. The total electron beam current was measured with a Faraday cup whose sensing element (1 cm^2 area) was located at the position that the specimen would normally occupy. The sensing element is connected to ground through a microammeter which measured the r.m.s. average electron beam current. Since space limitations did not permit measurement of the electron beam current during the specimen irradiations, it was necessary to record the appropriate accelerator control settings as a function of the measured Faraday cup current. This calibration was used to determine the electron current density during specimen irradiations. The experimental error associated with the determination of the electron current density incident on the specimen during any given irradiation was estimated to be ± 25 percent. This experimental error was attributed to the following factors:

1. Lack of repeatability of the accelerator control settings;

2. ionization of air due to electron beam resulting in additional source of current; and

3. slight differences in location and orientation of specimen and Faraday cup sensing element.

Specimen Configuration

The choice of a specimen configuration for the electron irradiation experiments were based on a large number of requirements which include:

1. obtaining the correct electron energy deposition that would result in the desired ionizing dose rates;

2. obtaining a sufficient optical path length through the specimen in order to allow accurate measurement of optical transmission;

3. minimizing the effects of thermally induced refractive index gradients in the specimen on the optical beam; and

4. minimizing the number of electrons stopping in the specimen which could result in induced birefringence or dielectric breakdown.

A suitable compromise among these various requirements was obtained by using a specimen in the form of a thin (1.5-mm) wafer of rectangular cross section. The specimen was mounted at an angle of 65 deg with respect to the electron beam axis and at an angle of 25 deg with respect to the optical beam axis as shown in Fig. 5.

The resulting optical path length at this angle was calculated to be 2 mm, which would yield a range of measurable absorption coefficients from 0.5 cm^{-1} to 23 cm^{-1}. The calculations to determine the ionizing dose rate and the fraction of the incident electrons stopped in the specimen are presented in Appendix B. These calculations indicate that approximately 25 percent of the incident electrons will be stopped in a 1.5-mm-thick specimen for an electron kinetic energy of 1.5 Mev. If the irradiations were conducted at ambient temperature, this would result in an enormous charge buildup in the specimen due to the large value of the electrical resistivity of fused silica ($\rho_e \sim 10^{18}$ ohm-cm) at room temperature. However, at elevated temperatures the resistivity decreases markedly due to an increase in ionic mobility. For example, the resistivity at 900 C is only 10^5 ohm-cm, a decrease of 13 orders of magnitude. A calculation of the induced charge density at 900 C and an electron current density of 150 microamps/cm^2 yields a value of approximately 10^{-11} coulomb/cm^3, which is far below that required for dielectric breakdown. Lichtenberg figures, characteristic of dielectric breakdown, were not observed in any of the irradiated specimens, indicating that the charge buildup was not significant.

The relation between the ionizing dose rate, $\dot{D}$, and the electron current density, J, for a specimen thickness of 1.5 mm and an electron kinetic energy, E, of

1.5 Mev as derived in Appendix B is:

$$\dot{D} = 1.34 \times 10^5 \, J(R/sec) \qquad (3)$$

with J expressed in microamperes/cm^2. This expression is, of course, approximate due to the extreme complexity of the atomic processes involved. However, the inaccuracy in this calculation should be less than the previously mentioned experimental error associated with the measurement of electron current density of ±25 percent. For this reason, the error associated with the determination of the ionizing dose rate will also be taken as ±25 percent. The ionizing dose rate expected in a full-scale NLB engine operating at a radiating temperature of 15000°R is given in Table I as 5.4×10^6 R/sec, which could be obtained in this specimen configuration with an electron current density of approximately 50 microamp/cm^2, well within the current capability of the Dynamitron Electron Accelerator.

The temperature of the specimen in the irradiated region was determined primarily by electron beam heating and, in fact, the resulting specimen temperatures were in close agreement with those expected from the calculated energy depositions. In order to provide additional heating, and a rigid supporting mount for the specimen, a furnace assembly was designed in which the specimen was mounted as shown in Fig. 5. This furnace was capable of maintaining the specimen at temperatures in the range (25 to 450 C) in the absence of electron beam heating. In order to obtain data in the temperature range of prime interest (600 to 900 C), it was necessary to conduct most of the irradiation at sufficiently high electron current densities (80 to 150 microamp/cm^2). A limited degree of temperature control was obtained by varying the furnace power, while temperature measurements were made with a thermocouple mounted on the back side of the specimen as shown in Fig. 5. The accuracy in the temperature measurement was estimated to be ±20 C. This was based on the inherent accuracy of the measuring equipment (±10 C) and the expected temperature difference between the thermocouple location and the point at which the optical transmission was measured (±10 C).

Optics and Electronic Systems

The light source used for these experiments was a Hanovia Model 771-B-32 hydrogen discharge lamp which provided the required light intensity in the wavelength range of interest (2150 to 4500 Å). The lamp was operated in a continuous-flow rather than a sealed configuration in order to prevent degradation of the output after extended operation. The light beam is apertured, collimated by an off-axis parabola (Perkin-Elmer 098-0041) and split by two plane mirrors into a specimen beam, S, and a reference beam, R, as shown in Fig. 5. The reference beam is included to account for variations in the source intensity and detector gain during the irradiation. Both beams are chopped sequentially resulting in a periodic light signal at a frequency of 13 Hz. The specimen beam is apertured a second time such that the light beam at the specimen has a rectangular cross section (2 mm x 5 mm) centered on the axis of the 1-cm-diameter electron beam. Both the specimen beam and the reference beam are collected and imaged by a second off-axis parabola on the

monochromator (Perkin-Elmer Model 99) as shown in Fig. 5. The light beams are monochromatized after passing through the specimen in order to prevent the broadband fluorescence generated by the specimen from saturating the photomultiplier tube (Ascop 543-1014). Extensive shielding of the photomultiplier tube was necessary in order to minimize the noise generated by x-rays incident on the cathode. In order to further discriminate against this souce of noise, as well as background light and specimen fluorescence, a phase sensitive detector, locked in phase with the sequential chopper, was used to extract the desired repetitive waveform out of a large noise background. The output of the phase-sensitive detector consists of two d-c signals, proportional to the intensity of the specimen beam and reference beam respectively. The two signals are amplified and their ratio (S/R) displayed on a chart recorder as a function of time during the irradiation. This electronic system has a response time of about 1 sec which sets the upper frequency measurement limitation to 1 Hz.

This system is capable of measuring optical transmission with an accuracy of ± 1 percent under controlled laboratory conditions. However, the additional noise environment encountered on site decreased the accuracy to ± 3 percent. This results in an accuracy in the measurement of induced absorption coefficient that varied from ± 16 percent at an induced absorption coefficient of 12 cm^{-1} to ± 17 percent at an induced absorption coefficient of 1.1 cm^{-1}.

Experimental Results

A total of 16 electron irradiations were conducted on a total of 8 specimens. Specimens D-1 through D-7 were used for actual optical transmission runs 2, 7, 8, 9, 10, 12, 13, 14, 15 and 16 while specimen D-8 was used for thermal and electronic calibration runs 1, 3, 4, 5, 6, and 11. The optical transmission runs were conducted at a wavelength of 2150 Å, with the exception of run 12 which was conducted at a wavelength of 4500 Å. The optical transmission and specimen temperatures were recorded before, during, and after each irradiation. The resulting irradiation-induced absorption coefficient at a given wavelength, λ, specimen temperature, T, ionizing dose rate, $\dot{D}$, and elapsed time, t, was calculated from the following equation:

$$\alpha = -\frac{1}{d_o} \ln \left[\frac{I(\lambda,T,\dot{D},t)}{I^o(\lambda)} \right] \qquad (4)$$

where:

α = irradiation-induced absorption coefficient (cm^{-1})

d_o = optical path length through specimen (cm)

$I^o(\lambda)$ = chart recorder amplitude before turn-on of electron beam

$I(\lambda,T,\dot{D},t)$ = chart recorder amplitude at a time t after turn-on of electron beam.

The electron current density, specimen temperature, and induced absorption coefficient for each of the 10 optical transmission runs are presented as functions of elapsed time in Figs. 6 through 15.

Figure 6 presents the results of run 12 in which the optical transmission of specimen D-3 was measured during the irradiation at a wavelength of 4500 Å, a current density of 80 microamp/cm^2 and an equilibrium temperature of 540 C. Except for a slight transient change in transmission during the onset of irradiation, there was no measurable steady state loss of transmission. This is expected, since Corning Grade 7940 fused silica does not have any strong irradiation-induced absorption bands at this wavelength. This result also indicates that the loss of signal due to thermally induced refractive index gradients in the specimen is negligible at this wavelength for the specimen configuration used. At the primary test wavelength of 2150 Å, the index of refraction varies more rapidly with temperature so that the effect of thermally induced refractive index gradients might be significant at this wavelength. However, it was not possible to measure the magnitude of this thermal effect at 2150 Å with the present optical system. It will, therefore, be assumed in this report that all changes in optical transmission were due to actual irradiation-induced absorption, until further experimental evidence indicates otherwise.

Figures 7 through 15 present the temporal behavior of the electron current density, the specimen temperature, and the irradiation-induced absorption coefficient for the irradiations conducted at 2150 Å, the primary wavelength of interest. The important aspects of the behavior of the induced absorption coefficient during these irradiations can be summarized as follows:

1. In all cases the irradiation-induced absorption coefficient reached a steady state value after the specimen temperature had reached equilibrium.

2. Decreasing the specimen temperature during the irradiation to a new equilibrium value caused the irradiation-induced absorption coefficient to rise to a higher steady state value, Figs. 11 and 12.

3. Increasing the specimen temperature during the irradiation to a new equilibrium value caused the irradiation-induced absorption coefficient to decrease to a lower steady state value, Fig. 14.

4. A simultaneous increase in electron current density and specimen temperature caused the induced absorption coefficient to rise to a higher steady state value, Figs. 11 and 13.

5. In certain of the irradiations, the induced absorption coefficient was observed to rise to a maximum value before returning to a lower equilibrium value, Figs. 7, 8, 9, 11 and 14.

6. After the electron beam was turned off, the induced absorption coefficient decreased rapidly; in some cases the induced absorption coefficient reached a minimum value and then increased to a slightly higher final value, Figs. 7, 8, 11, 12 and 13. This apparent "overshoot" anomaly is believed to be due to the slow response of the chart recorder rather than any actual physical effect.

The above behavior can be interpreted using the models of color center generation derived in Appendix A and discussed in the first section of this report. These models predict that the induced absorption coefficient will reach an equilibrium value that is a decreasing function of temperature (due to thermal bleaching and annealing), and an increasing function of ionizing dose rate. The temporal variation of the irradiation-induced absorption coefficient described above is also in qualitative agreement with the predictions of Appendix A. The form of the predicted rise of the induced absorption coefficient to its final equilibrium value due to a constant ionizing dose rate are illustrated in Figs. 16 and 17.

Figure 16 illustrates a solution of the rate equations derived in Appendix A in which the defects are assumed to be generated by the incident radiation and in which the specimen temperature is assumed constant, and indicates an induced absorption coefficient that rises steadily to equilibrium. Figure 17 illustrates two solutions of the rate equations derived in Appendix A in which a fixed concentration of defects are assumed. Curve A of Fig. 17 is a solution for which the specimen temperature is assumed constant during the irradiation, and indicates an induced absorption coefficient that rises steadily with time to equilibrium. Curve B of Fig. 17 is a solution for which the specimen temperature is assumed to rise to a final equilibrium value during the irradiation. The induced absorption coefficient rises to a maximum value before returning to a lower equilibrium value, thus providing an explanation of the phenomena illustrated in Figs. 7, 8, 9, 11 and 14.

A quantitative analysis of the temporal behavior of the induced absorption coefficient is of limited value and is extremely difficult due to the variation of the specimen temperature during the transient period. However, the equilibrium values of induced absorption coefficient are simple to interpret and are of primary importance, since the nominal running time of the engine (1000 sec) is much longer than the rise times measured in these experiments ($\sim$ 100 sec).

The measured equilibrium values of the irradiation-induced absorption coefficient at 2150 Å for specimens D-1 through D-7 are plotted against specimen temperature for the different values of electron current density in Fig. 18. The error bars shown are those due to the error in the measurement of optical transmission ($\pm$3 percent) and do not include the error in the measurement of temperature ($\pm$20 C) and the measurement of electron current density ($\pm$25 percent). Within the overall experimental error, the equilibrium values of induced absorption coefficient are observed to increase with increasing current density and decrease with increasing temperature, as expected.

REACTOR IRRADIATION EXPERIMENTS

Measurements of the optical transmission of Corning Grade 7940 fused silica over a range of specimen temperature and at two optical wavelengths during steady-state nuclear reactor irradiation were performed at the Nuclear Engineering Center of the Air Force Institute of Technology located at Wright-Patterson Air Force Base, Dayton, Ohio. The experiments were performed using the Center's 10-megw swimming pool reactor as a source of fast neutrons and gamma rays to simulate the radiation damage effects in the transparent wall of a nuclear light bulb rocket engine. Table I gives a comparison of the radiation levels for this and previous experiments as well as the most recent predicted radiation levels for the transparent wall of a full-scale nuclear light bulb engine. The radiation levels (supplied by Wright-Patterson Air Force Base personnel) for the present experiments are the nominal values obtained at the location of the specimen at full reactor power (10 megw). Both the ionizing dose rate due to gamma rays and the fast neutron flux vary linearly with reactor power down to a reactor power of about 0.1 megw. Thus, the ionizing dose rate at half-power (5 megw) is 1×10^4 R/sec at the location of the specimen. Of interest also is the neutron energy spectrum for the reactor which is plotted in normalized form with the expected neutron energy spectrum of the full scale engine in Fig. 19.

Description of Experiment and Test Procedure

Figure 20 is a combined electrical and optical schematic that illustrates in functional form the important experimental equipment with their respective locations. The radiation area for these experiments was the East Test Cell which is located directly adjacent to the reactor core as shown in Fig. 20. The variation of the ionizing dose rate at a reactor power of 10 megw with position in this area and the location of the corner cube specimen are illustrated in Fig. 21. The furnace assembly, which was previously used in the TRIGA experiments (Ref. 10), was located as shown in Fig. 20, and provided a rigid supporting mount for the specimen, as well as elevated specimen temperatures. Due to the high radiation level in the area adjacent to the test cell with the shielding door open and the reactor off, it was necessary to insert the furnace assembly by mounting it on a cart that was then remotely driven into the test cell area. After insertion of the furnace assembly, the shielding door was closed and remained closed for the duration of the experiment. A 2 5/16 in.-dia hole in the shielding door, which allowed the insertion of the specimen and specimen holder, provided the necessary optical line-of-sight to the specimen.

The specimen holder consisted of a 12-in. alundum cylinder, in which the specimen is seated, which is then mounted on a 20-ft aluminum tube. The specimen holder is inserted through the 2 5/16-in.-dia hole in the shielding door until the specimen comes in contact with a pair of thermocouples in the furnace assembly. The furnace and thermocouple leads were brought out of the test cell through overhead plugs to the reactor upper levels where the recording and control equipment was located. One of the thermocouples was used to provide a direct temperature readout

while the second thermocouple was used to provide the feedback signal for the furnace controller that provided temperature regulation of ±1 C at any preset temperature in the range from 225 to 900 C.

The optical table, containing the source, detector and optical components, was located approximately 10 ft from the 2 5/16-in.-dia hole in the shielding door. The light beam from the hydrogen lamp source (Hanovia 771-B-32) is collimated by mirror M_1 (Perkin-Elmer 098-0041) and split into a specimen beam and a reference beam by a beam splitter as shown in Fig. 20. The reference beam is reflected successively off mirrors M_4, M_3, M_5 and focussed by M_6 (Perkin-Elmer 098-0041) onto the entrance slit of the monochromator (Perkin-Elmer 99). The specimen beam passes through the beam splitter and is reflected off of mirror M_7 which is mounted on the end of the specimen holder. The reflected beam then passes down the tube to a corner cube specimen and is reflected back on itself. The specimen beam is then successively reflected off mirror M_7, the beam splitter, and mirrors M_3, M_5 and M_6, and is then incident on the entrance slit of the monochromator. A series of four automatically actuated shutters, S1, S2, S3 and S4 in Fig. 20 were used in order to successively detect the zero level, the specimen beam, the reference beam and the specimen fluorescence. The period of this sequence was 1 min. No specimen fluorescence or change in the zero level was detected during the experiments, but changes in the reference and specimen beams due to slow variations in the output of the hydrogen lamp were observed, which corroborated the necessity of a dual-beam system for these experiments.

A particular wavelength is selected from the continuous spectrum of the hydrogen lamp by the monochromator, whose output is then detected by the photomultiplier tube (Ascop 543-1014). The resulting electrical signal is amplified and used as the input to a chart recorder which then gives a permanent record of the relative amplitude of the zero level, specimen beam, reference beam and specimen fluorescence as a function of elapsed time during the irradiation. The experimental accuracy associated with the measurement of optical transmission was assumed to be equal to the value of ±1 percent obtained under controlled laboratory conditions. This was due to the negligible amount of noise encountered on site in these experiments as compared with the electron irradiation experiments. This error in optical transmission results in an error in the irradiation-induced absorption coefficient of ±17 percent at an absorption coefficient of 0.01 cm^{-1} and ±3.5 percent at an absorption coefficient of 0.3 cm^{-1} with the optical path length of 6.25 cm associated with the corner cube specimen.

Experimental Results

The resulting irradiation-induced absorption coefficient at a given wavelength, λ, specimen temperature, T, ionizing dose rate, D, and elapsed time, t, is calculated from the following equation:

$$\alpha = -\frac{1}{d_o} \ln \left[\frac{I_s(\lambda,T,\dot{D},t)}{I_r(\lambda,t)} \cdot \frac{I_r^{\circ}(\lambda)}{I_s^{\circ}(\lambda,T)} \right] \qquad (5)$$

where:

α = irradiation-induced absorption coefficient (cm^{-1})

d_o = path length through specimen (cm)

$I_s(\lambda,T,\dot{D},t)$ = specimen beam amplitude at wavelength, λ, temperature, T, ionizing dose rate, $\dot{D}$, and elapsed time, t, during irradiation

$I_r(\lambda,T)$ = reference beam amplitude at wavelength, λ, and elapsed time, t

$I_s^{\circ}(\lambda,T)$ = specimen beam amplitude at wavelength, λ, and temperature, T, prior to reactor start-up

$I_r^{\circ}(\lambda)$ = reference beam amplitude at wavelength, λ, prior to reactor start-up.

A total of three specimens were irradiated on three consecutive weeks (one specimen per week), and the optical transmission was measured as a function of specimen temperature, ionizing dose rate and time during the irradiation. The first two runs were made at a wavelength of 2150 Å, while the third and final run was made at a wavelength of 2700 Å. Figures 22, 23 and 24 present the ionizing dose rate and specimen temperature during the irradiation for specimens R-1, R-2 and R-3, respectively. As shown in Figs. 22 and 23, the temperature of specimen R-1 was maintained at 900 C during the overnight periods while specimen R-2 was maintained at 250 C during the same periods. The measured values of equilibrium induced absorption coefficient as functions of specimen temperature and elapsed time during the irradiation are presented in Figs. 25, 26, and 27 for specimens R-1, R-2 and R-3, respectively. Curves A, B, C and E in Fig. 25 are plots of induced absorption coefficient vs. specimen temperature at an ionizing dose rate of 2×10^4 R/sec and a wavelength of 2150 Å for specimen R-1. It is observed that the curves are lower for increasing elapsed time during the run. This would indicate either a systematic experimental error due to a shift in the optical alignment or a definite slow decrease in absorption coefficient which was only observable over long periods of time. Curve D is a plot of the induced absorption coefficient vs. specimen temperature at an ionizing dose rate of 1×10^4 R/sec for specimen R-1. As expected, Curve D is lower than curves A, B, C, and E.

Curve D in Fig. 26 is a plot of equilibrium induced absorption coefficient vs. specimen temperature at an ionizing dose rate of 2×10^4 R/sec and a wavelength of 2150 Å for specimen R-2. Points B, C and E are additional values obtained at different times during the irradiation at the same ionizing dose rate for a specimen temperature of 900 C. It is observed that points E and D, measured at the end of the run, are higher than points B and C, measured earlier in the run. This is in contrast to the behavior of the induced absorption coefficient for specimen R-1, where the absorption coefficient at a given temperature was observed to decrease with increasing time. This behavior might be due to the different temperature histories of the two specimens (See Figs. 22 and 23) or to systematic or random experimental errors. Point A of Fig. 26 is the equilibrium induced absorption coefficient at an ionizing dose rate of 1×10^4 R/sec, a wavelength of 2150 Å, and a specimen temperature of 900 C. As expected, the induced absorption coefficient is lower than the corresponding values at 2×10^4 R/sec.

Figure 27 is a curve of equilibrium induced absorption vs. specimen temperature at an ionizing dose rate of 2×10^4 R/sec and a wavelength of 2700 Å for specimen R-3. Since this wavelength is not at the center of an irradiation-induced absorption band, this curve lies below the corresponding curves at a wavelength of 2150 Å for specimens R-1 and R-2.

If the data at a given ionizing dose rate, wavelength and temperature are averaged arithmetically, the following average values at 900 C are obtained. The average equilibrium induced absorption coefficient at an ionizing dose rate of 2×10^4 R/sec, a wavelength of 2150 Å and a specimen temperature of 900 C is 0.034 cm^{-1}. The average equilibrium induced absorption coefficient at an ionizing dose rate of 1×10^4 R/sec, a wavelength of 2150 Å and a specimen temperature of 900 C is 0.015 cm^{-1}. This is approximately a factor of 2 lower than the value at 2×10^4 R/sec, indicating that the induced absorption coefficient varies approximately linearly with ionizing dose rate. The equilibrium induced absorption coefficient at an ionizing dose rate of 2×10^4 R/sec, a wavelength of 2700 Å and a specimen temperature of 900 C is 0.01 cm^{-1} which, as expected, is lower than the corresponding value at 2150 Å.

DISCUSSION OF RESULTS

Representative data showing the equilibrium values of the irradiation-induced absorption coefficient at 2150 Å measured in both experiments are tabulated in Table II and plotted against ionizing dose rate at temperatures of 700 C, 800 C, and 900 C in Fig. 28. Also plotted in Fig. 28 are calculated curves based on the following limiting form of the equations derived in Appendix A and discussed previously in the text.

$$\alpha_{calc} = g\dot{D}\tau \qquad (6)$$

The generation rate due to ionizing radiation was taken as 0.045 cm^{-1}/Mrad on the basis of the ambient-temperature Co-60 irradiation experiments (Fig. 2); and the thermal decoloration time constant, τ, was taken from post-reactor thermal decoloration data (Fig. 3). It can be seen from Table II and Fig. 28 that the calculated absorption coefficients are in reasonable agreement with the absorption coefficients measured in the reactor experiments. However, the calculated absorption coefficients are consistently higher than the corresponding absorption coefficients measured in the electron irradiation experiments and agreement was obtained only to within an order to magnitude. This discrepancy may have been due to large experimental errors in the electron irradiation experiments, an actual saturation of the induced absorption at high ionizing dose rates, or some fundamental difference between the ionizing effects due to gamma rays and those due to electrons. Further experiments will be necessary to resolve this discrepancy. The ionizing dose rate expected in the full-scale NLB engine operating at a radiating temperaure of 15,000 R is given in Table II as 5.4×10^6 R/sec and is indicated in Fig. 28 by the dashed vertical line. A prediction based on either the calculated curves or a linear extrapolation of the results of the reactor experiments yields a value of 8.3 cm^{-1} at a temperature of 900 C for this ionizing dose rate. The results of the electron irradiation experiments indicate a somewhat lower value ($\sim$3 cm^{-1}) but a meaningful extrapolation from this data does not seem justified at this time.

The value of 8.3 cm^{-1} of induced absorption that is predicted for the full-scale engine on the basis of the present experiments is a pessimistic one in that the effects of optical bleaching were not included in any of the experiments. To investigate this effect, a preliminary experiment was performed in which a specimen, which had been previously colored by electron irradiation, was exposed to ultraviolet light from a hydrogen lamp. The time for the induced absorption coefficient at 2150 A to decay to 1/e of its initial value was measured and found to be 4800 sec. Since the photon flux in the wavelength range of interest was 10^{-7} of that expected in a full-scale nuclear rocket engine, and since the time constant for optical bleaching is inversely proportional to photon flux, the expected optical bleaching time constant in the engine is approximately 0.48×10^{-3} sec. This corresponds to a decoloration rate due to optical bleaching, cI, of approximately 2×10^4 sec^{-1}.

As derived in Appendix A, the expected decrease in the induced absorption coefficient due to the addition of optical bleaching is given by the multiplying factor:

$$\beta = \frac{b\dot{D} + 1/\tau}{b\dot{D} + \frac{1}{\tau} + cI} \tag{7}$$

where:

$b\dot{D}$ = coloration rate due to trapping of electrons by defects (sec^{-1})

$\frac{1}{\tau}$ = thermal decoloration rate (sec^{-1})

cI = optical bleaching decoloration rate (sec^{-1})

This relation is plotted as a function of cI for several values of $(b\dot{D} + 1/\tau)$ in Fig. 4. It is apparent from an examination of Eq. (6) and Fig. 4 that optical bleaching will result in a significant decrease in the induced absorption expected in the full-scale engine if:

$$b\dot{D} + \frac{1}{\tau} << cI = 2 \times 10^4 \ sec^{-1} \tag{8}$$

It is difficult to estimate the quantity on the left hand side of the above inequality with the available experimental data. This estimate is critically dependent on knowledge of which of the two models describing the coloration process, as discussed in Appendix A, is dominant. If the coloration process is due mainly to the filling of existing defects by electrons, then the term on the left hand side of the inequality will be approximately equal to the time constant for the induced absorption to reach equilibrium. The results of the electron irradiation experiments indicate that this time constant is on the order of 100 sec, so that in this case the inequality would be satisfied by several orders of magnitude. However, if the coloration process is due mainly to the filling of defects that are generated by the incident radiation, the situation is considerably more complex and a meaningful estimate cannot be obtained from the present data. Further experimentation will be necessary in order to make a meaningful estimate of the effects of optical bleaching in limiting the induced absorption in the transparent wall of the nuclear light bulb rocket engine.

REFERENCES

1. Latham, T. S.: Nuclear Studies of the Nuclear Light Bulb Rocket Engine. United Aircraft Research Laboratories Report G-910375-3, September 1968. Also issued as NASA CR-1315.

2. Dienes, G. J.: Defects in Silicas. J. Phys. Chem. Solids. 13, 272 (1960).

3. Levy, P. W.: Reactor and Gamma-Ray Induced Coloring in Crystalline Quartz and Corning Fused Silica. J. Chem. Phys. 23, 764 (1955).

4. Levy, P. W.: Reactor and Gamma-Ray Induced Coloring of Corning Fused Silica. J. Phys. Chem. Sol. 13, 287 (1960).

5. Compton, W. D. and G. W. Arnold, Jr.: Radiation Effects in Fused Silica and α-Al_2O_3. Disc Faraday Soc. 31, 130 (1961).

6. Nelson, C. M. and J. H. Crawford, Jr.: Optical Absorption in Irradiated Quartz and Fused Silica. J. Phys. Chem. Sol. 13, 296 (1960).

7. Douglas, F. C. and R. M. Gagosz: Experimental Investigation of Thermal Annealing of Nuclear-Reactor-Induced Coloration in Fused Silica. UARL Contract Report D910082-7. Also issued as NASA CR-304.

8. Gagosz, R. M., F. C. Douglas and M. A. DeCrescente: Optical Absorption in Transparent Materials Following High-Temperature Reactor Irradiation. United Aircraft Research Laboratories Report F-910485-2, September 1967. Also issued as NASA CR-1032.

9. Gagosz, R. M., J. P. Waters, F. C. Douglas and M. A. DeCrescente: Optical Absorption in Fused Silica During Triga Reactor Pulse Irradiations. United Aircraft Research Laboratories Report F-910485-1, September 1967. Also issued as NASA CR-1031.

10. Gagosz, R. M. and J. P. Waters: Optical Absorption and Fluorescence in Fused Silica During Triga Pulse Irradiation. United Aircraft Research Laboratories Report G-910485-3, April 1968. Also issued as NASA CR-1191.

11. Burrell, M. O., J. J. Wright and J. W. Watts, Jr.: The Calculation of Electron and Bremsstrahlung Dose Rates. In Protection Against Space Radiation NASA SP-169, pg. 529-538.

LIST OF SYMBOLS

a	Defect generation constant, cm^{-3}-$Mrad^{-1}$
b	Electron trapping constant, $Mrad^{-1}$
c	Optical bleaching constant, $watts^{-1}$-cm^2 sec^{-1}
$\dot{D}$	Ionizing dose rate, Mrad/sec
d	Specimen thickness, cm.
d_o	Optical path length through specimen, cm
E	Neutron or electron kinetic energy, Mev
g	Generation rate due to ionizing radiation, cm^{-1}/Mrad
I	Light intensity, watts/cm^2
$I(\lambda,T,\dot{D},t)$	Chart recorder amplitude during electron irradiation, dimensionless
$I^o(\lambda)$	Chart recorder amplitude before turn on of electron beam, dimensionless
$I_r(\lambda,t)$	Reference beam amplitude during reactor irradiation, dimensionless
$I_r^o(\lambda)$	Reference beam amplitude prior to reactor start up, dimensionless
$I_s(\lambda,T,\dot{D},t)$	Specimen beam amplitude during reactor irradiation, dimensionless
$I_s^o(\lambda,T)$	Specimen beam amplitude prior to reactor start up, dimensionless
J	Electron current density, microamp/cm^2
$N_c^{(eq)}$	Equilibrium color center concentration, cm^{-3}
N_d	Defect concentration, cm^{-3}
N_d^o	Fixed concentration of defects, cm^{-3}
$R(E)$	Electron range, cm
x	Dimensionless range parameter

T	Specimen temperature, deg C
$\alpha(\lambda)$	Induced absorption coefficient at a wavelength, λ, cm^{-1}
α_{calc}	Calculated induced absorption coefficient, cm^{-1}
β	Optical bleaching multiplying factor, dimensionless
λ	Optical wavelength, Å
η	Fraction of incident electrons stopped, dimensionless
ω	Electron beam radius, cm
ρ	Density, $gm\text{-}cm^{-3}$
ρ_e	Electrical resistivity, ohm-cm
$\sigma_{ph}(\lambda)$	Optical absorption cross section at a wavelength, λ, cm^2
τ	Thermal decoloration time constant, sec
τ_A	Thermal annealing time constant, sec
τ_B	Thermal bleaching time constant, sec
τ_R	Thermal bleaching rise time, sec
Θ	Electron beam divergence angle, degrees
ξ	Fraction of incident electron energy deposited, dimensionless

APPENDIX A

KINETIC EQUATIONS FOR COLOR CENTER GENERATION

Differential equations based on a first order kinetic approximation have been derived for the temporal variation of the concentration of color centers during irradiation. Since the induced absorption coefficient is directly proportional to the concentration of color centers, the solutions of these equations can be directly related to the experimental results. Several approximations were made in the derivation in order to obtain a tractable mathematical model. These include neglecting the effects of neutron damage, and assuming that the generation, bleaching and annealing of color centers are all first-order processes. Equations were derived for two specific cases corresponding to two distinct models of the coloration process: 1- defect generation produced by ionizing radiation and; 2- a fixed concentration of defects.

Defect Generation by Ionizing Radiation

In this case defects are generated due to rupturing of molecular bonds by the ionizing radiation. Free electrons are also generated by the ionizing radiation which are then trapped by the defects resulting in the formation of color centers. Annihilation of color centers results from both bleaching and annealing processes. Two different equations, one for the concentration of defects, and one for the concentration of color centers due to trapping at these defects, are required. They are:

$$\frac{d\,Nd}{dt} = a\dot{D} - \frac{Nd}{\tau_A} \qquad (A\text{-}1)$$

and

$$\frac{dN_c}{dt} = b\dot{D}\,(N_d - N_c) - \frac{N_c}{\tau_B} - \frac{N_c}{\tau_A} \qquad (A\text{-}2)$$

where:

$\dot{D}$ = ionizing dose rate (Mrad/sec)

N_d = concentration of defects (cm^{-3})

N_c = concentration of color centers (cm^{-3})

a = defect generation constant (cm^{-3} - $Mrad^{-1}$)

b = electron trapping constant ($Mrad^{-1}$)

τ_A = annealing time constant (sec)

τ_B = thermal bleaching time constant (sec)

The steady state value of the color center concentration is found by setting all the derivatives equal to zero and solving for N_c. The result for this case is:

$$N_c^{(eq)} = \frac{b\dot{D}}{b\dot{D} + \frac{1}{\tau_B} + \frac{1}{\tau_A}} a\dot{D}\tau_A \qquad \text{(A-3)}$$

$$= \begin{bmatrix}\text{Fraction of defects that} \\ \text{have trapped electrons}\end{bmatrix} \times \begin{bmatrix}\text{Equilibrium concentration} \\ \text{of defects}\end{bmatrix}$$

If the ionizing dose rate is large enough that, $b\dot{D} >> \frac{1}{\tau_A} + \frac{1}{\tau_B}$, then the defects are all filled with electrons. The resulting "saturated" color center concentration is given by:

$$N_c^{(eq)} = a\dot{D}\tau_A \qquad \text{(A-4)}$$

In order to examine the nature of the approach to equilibrium the solutions of Eqs. (1) and (2) were obtained for several different values of the parameters a, b, τ_A, τ_B and D. Figure 16 is a normalized plot of a representative solution of the equations where the ionizing radiation is turned on at t = 0 and the specimen temperature is assumed constant during the irradiation. The following values of the parameters were used:

$b\dot{D} = 10^4 \text{ sec}^{-1}$

$\tau_A = 100$ sec

$\tau_B = 1$ sec

It was implicitly assumed that the time constants, τ_A and τ_B, were independent of time. However, this may not be the case in an actual experimental situation since τ_A and τ_B are functions of temperature. The specimen temperature may be changing with time due to direct heating by the ionizing radiation, thus causing τ_A and τ_B to be functions of time also.

Fixed Concentration of Defects

In this case a fixed concentration of defects is present in the specimen due to intrinsic disorder in the glass structure. The incident radiation does not create defects but does generate free electrons which are then trapped by the existing

defects. Annihilation of color centers results from bleaching processes only since the intrinsic defects do not anneal. A single differential equation is required in this case.

$$\frac{dN_c}{dt} = b\dot{D}(N^\circ_d - N_c) - \frac{N_c}{\tau_B} \qquad \text{(A-5)}$$

where N_d° is the fixed concentration of defects. The steady state value of the color center concentration is:

$$N_c^{(eq)} = \frac{b\dot{D}}{b\dot{D} + \frac{1}{\tau_B}} N_d^\circ \qquad \text{(A-6)}$$

$$N_c(eq) = \begin{bmatrix}\text{Fraction of defects that have}\\ \text{trapped electrons}\end{bmatrix} \times \begin{bmatrix}\text{Fixed concentration of}\\ \text{defects}\end{bmatrix}$$

If the bleaching process is rapid enough that $b\dot{D} << \frac{1}{\tau_B}$, then the color center concentration has the same form as Eq. (A-4) which was derived from a different model.

$$N_c^{(eq)} = bN^\circ_d \dot{D}\tau \qquad \text{(A-7)}$$

In order to examine the nature of the approach to equilibrium, the solution of Eq. (A-5) was obtained for several different values of the parameters b, $\frac{1}{\tau_B}$ and D. Curve A of Fig. 17 is a representative solution of Eq. (A-5) for the case of constant specimen temperature. The following values of the parameters were used.

$$b\dot{D} = 10^{-2}\ \text{sec}^{-1}$$

$$\tau_B = 10\ \text{sec}$$

A solution of Eq. (A-5) was also obtained in which the bleaching time constant was the following function of time.

$$\frac{1}{\tau(t)} = \frac{1}{\tau_B}\left(1 - e^{-t/\tau_r}\right) \qquad \text{(A-8)}$$

This would correspond qualitatively to the case in which the specimen was at ambient temperature at t = 0 for the which the bleaching time constant is essentially infinite, and then rises to a final temperature due to radiation heating, for which the bleaching time constant is τ_B. This solution is plotted as curve B in Fig. 28. The following values of the parameters were used:

$$b\dot{D} = 10^{-2}\ \text{sec}^{-1}$$

$$\tau_B = 10\ \text{sec}$$

$$\tau_R = 10\ \text{sec}$$

This curve exhibits a definite maximum similar to those observed in the results of the electron irradiation experiments and thus provides an explanation for this phenomenon.

Optical Bleaching

Optical bleaching by light of intensity I (watts/cm^2) adds a term on the right hand side of Eqs. (A-2) and (A-5) of the form:

$$\left.\frac{dN_c}{dt}\right|_{\text{optical bleaching}} = -cIN_c \qquad \text{(A-9)}$$

where c is a constant that depends on the overlap of the spectral distribution of the bleaching light with the spectral distribution of the absorption band. This results in a decrease in the equilibrium concentration of color centers by a factor β, where:

$$\beta = \frac{b\dot{D} + 1/\tau}{bD + \frac{1}{\tau} + cI} \qquad \text{(A-10)}$$

where:

$b\dot{D}$ = electron trapping rate (sec^{-1})

$1/\tau$ = thermal bleaching and annealing rate (sec^{-1})

cI = optical bleaching rate (sec^{-1})

The function β is plotted in Fig. 4 vs. the optical bleaching rate for several values of $(b\dot{D} + 1/\tau)$. The optical bleaching rate can be obtained experimentally by measuring the decay of the induced absorption at ambient temperature of a previously irradiated specimen due to bleaching by a light source of known intensity and spectral distribution. The decay is a simple exponential whose time constant is just the inverse of the optical bleaching rate.

APPENDIX B

IONIZING DOSE RATE CALCULATION FOR ELECTRON IRRADIATION IN THICK SPECIMENS

The problem of calculating the ionizing dose rate due to the passage of relativistic electrons through thick specimens (specimen thickness comparable to the range of the electron) is complicated due to the large "straggling" of the electron energy and the increase in electron path length due to inelastic scattering. These two effects result in a broad distribution of electron energy loss. In order to calculate the energy deposited in the specimen, which can then be converted to ionizing dose rate, it is necessary to average the energy loss over this distribution. A recently developed semi-empirical technique, given in Ref. 11 and based on a Monte-Carlo analysis, agrees well with experiment and is the one used in this report. The fraction of the incident electron energy deposited, ξ, and the fraction of the incident electrons stopping in the specimen, η, are given by the following semi-empirical equations:

$$\xi = 0.95 \left[1 - \exp\left(-.653x - 2.40x^2 - 6.89x^3\right)\right] \qquad \text{(B-1)}$$

$$\eta = 0.912 \left[1 - \exp\left(-.0512x + 1.128x^2 - 9.38x^3\right)\right] \qquad \text{(B-2)}$$

where:

$$x = \frac{d}{(1.33 - 0.19E)R(E)} = \text{dimensionless range parameter.}$$

d = specimen thickness (cm)

E = electron kinetic energy (Mev)

R(E)= electron range (cm)

Both of these expressions are plotted in Fig. 29 vs. the dimensionless variable x. The choice of a specimen thickness, d, and an electron energy, E, determines x, which in turn determines the energy deposition and the fraction of electrons stopped in the specimen. It is desirable to make ξ as large as possible, in order to obtain a sufficient dose rate, while keeping η as small as possible to minimize the charge buildup in the specimen. These two requirements are contradictory and a compromise must be made in the choice of x. In addition, the thickness must be large enough to permit accurate measurement of optical transmission ($d > 1$ mm) and the electron energy must be within the operating range of the accelerator ($E < 3$ Mev). Based on these considerations a specimen thickness of 1.5 mm, and an electron energy of 1.5 Mev were chosen. The range of a 1.5 Mev electron in fused silica is $R(E) = 4$ mm;

so that the dimensionless parameter, x, becomes 0.36. Substituting into Eqs. (1) and (2) $\xi = 0.54$ and $\eta = 0.25$. Thus, 54 percent of the energy and 25 percent of the electrons will be absorbed in a 1.5 mm slab of fused silica when the incident electrons have a kinetic energy of 1.5 Mev. The resulting ionizing dose rate is given by the following equation:

$$\dot{D} = \xi\left(\frac{JE}{\rho d}\right)\left[1 + \tan\theta\left(\frac{d}{\omega} + \frac{1}{3}\frac{d^2}{\omega^2}\tan\theta\right)\right]^{-1} \times 10^5 \left(\frac{\text{Rad}}{\text{sec}}\right) \qquad \text{(B-3)}$$

where:

$\dot{D}$ = ionizing dose rate (Rad/sec)

$\xi = 0.54$

J = electron current density (microamp/cm^2)

ρ = density of fused silica - 2.2 gm/cm^2

d = specimen thickness - 0.15 cm

E = electron energy - 1.5 Mev

θ = electron beam angle of divergence $\sim 60°$

ω = electron beam radius - 0.5 cm

Numerically, this reduces to

$$\dot{D} = 1.34\ J \times 10^5 \text{ (Rad/sec)}$$

Thus, at a current density of 150 microamp/cm^2, the ionizing dose rate is 2×10^7 R/sec.

TABLE I

NOMINAL RADIATION LEVELS FOR VARIOUS EXPERIMENTS
AND FOR FULL-SCALE NUCLEAR LIGHT BULB ENGINE

(a) Ionizing Radiation Levels

EXPERIMENT	IONIZING DOSE RATE (R/sec)	RUN TIME (sec)	IONIZING DOSE (R)
TRIGA	6.1×10^{7}	0.033	2.0×10^{6}
DYNAMITRON†	2.0×10^{7}	10^{3}	2.0×10^{10}
WPAFB	2.0×10^{4}	3.5×10^{5}	7.0×10^{9}
NLB (T*=15,000 R)	5.4×10^{6}	10^{3}	5.4×10^{9}

(b) Fast Neutron Radiation Levels; E > 0.75 Mev

EXPERIMENT	FAST NEUTRON FLUX (n/cm^2-sec)	RUN TIME (sec)	TOTAL NEUTRON DOSE (n/cm^2)
TRIGA	1.85×10^{15}	0.042	0.79×10^{14}
WPAFB	1.7×10^{12}	3.5×10^{5}	5.9×10^{18}
NLB (T*=15,000 R)	2.0×10^{15}	10^{3}	2.0×10^{18}

† See Appendix B

TABLE II

COMPARISON OF EXPERIMENTAL AND CALCULATED VALUES OF IRRADIATION-INDUCED ABSORPTION COEFFICIENT AT 2150 Å

$$\alpha_{calc} = g\dot{D} \times \tau$$

$$g = 0.045 \text{ cm}^{-1}/\text{Mrad}$$

Experiment or Engine	Wall Temp. deg C	Dose Rate $\dot{D}$,(Mrad/sec)	Time Constant from Post-Irradiation Exp. of Ref. 8 τ(sec)	Calculated Absorption Coefficient α_{calc} (cm^{-1})	Experimentally Determined Absorption Coefficient α(cm^{-1})
DYNAMITRON	900	20.0	34	31	12.0
	800	16	58	42	3.9
	700	10.5	61	29	5.0
WPAFB	900	0.02	34	0.031	0.034
	800	0.02	58	0.052	0.050
	700	0.02	61	0.055	0.054
NLB (T* = 15,000 R)	900	5.4	34	8.3	

H-930709-1

FIG. 1

TRANSMITTANCE SPECTRA OF 30 mm CORNING FUSED SILICA SPECIMEN SC 30-113, CONTROL, RECEIVED FROM VENDOR HEATED AT 1050 C, AND SUBSEQUENTLY Co-60 GAMMA DOSED

SPECIMEN THICKNESS = 30 mm
DATA FROM REF. 8

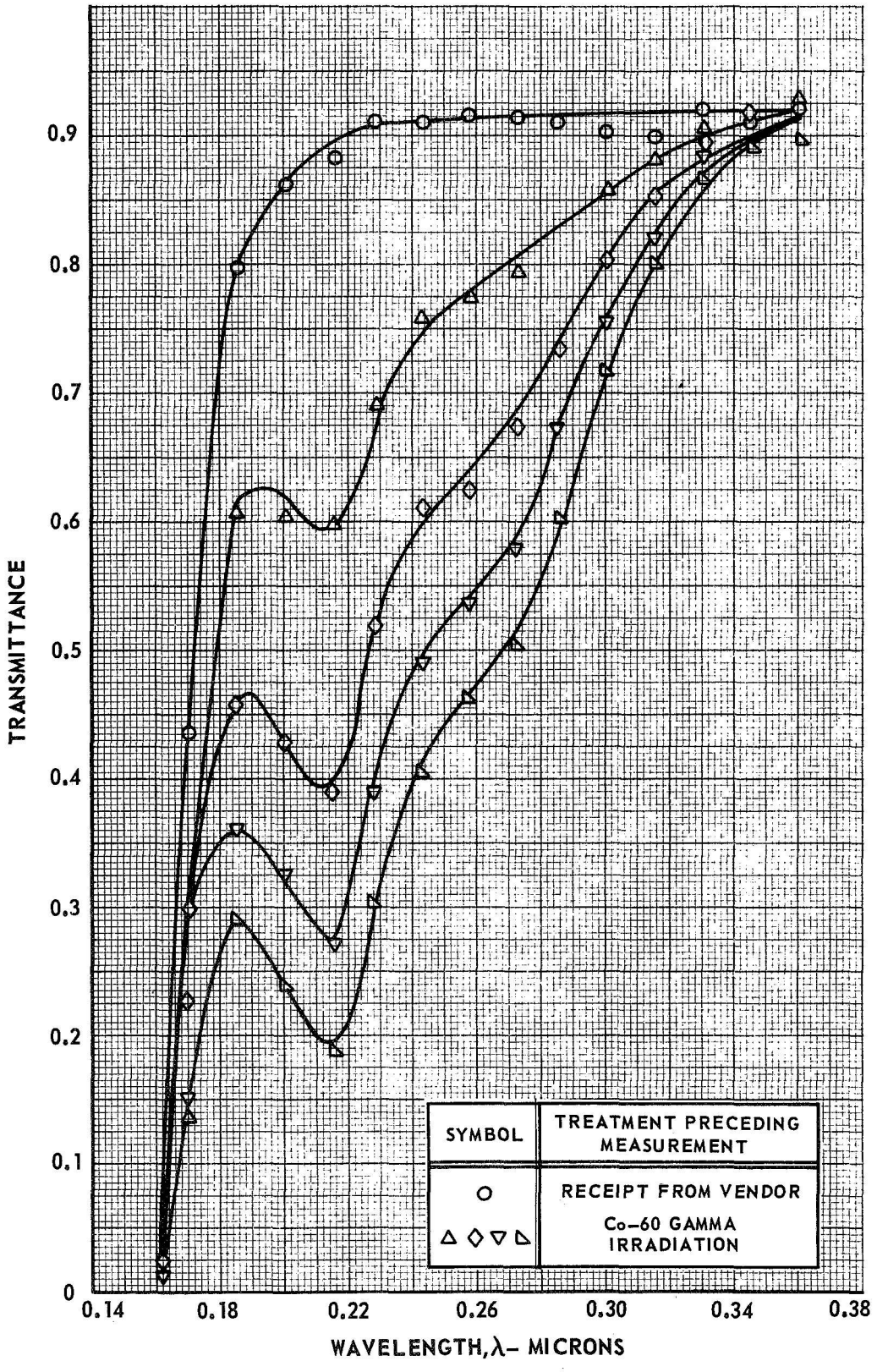

FIG. 2

GROWTH OF INDUCED ABSORPTION COEFFICIENT DURING AMBIENT TEMPERATURE Co-60 IRRADIATION

DATA FROM REF. 8

$\lambda = 2150$ Å

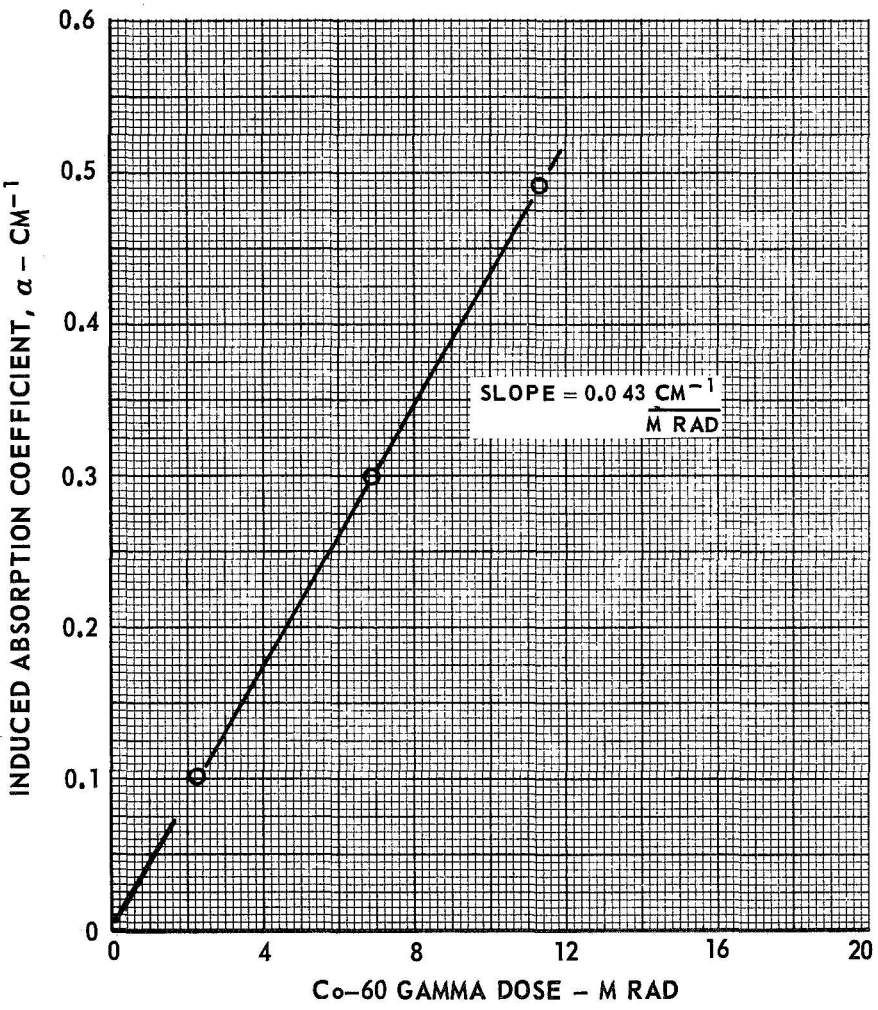

FIG. 3

TIME CONSTANT FOR REMOVAL OF REACTOR-INDUCED ABSORPTION AT ELEVATED TEMPERATURES

DATA FROM REF. 8

λ= 2150 Å

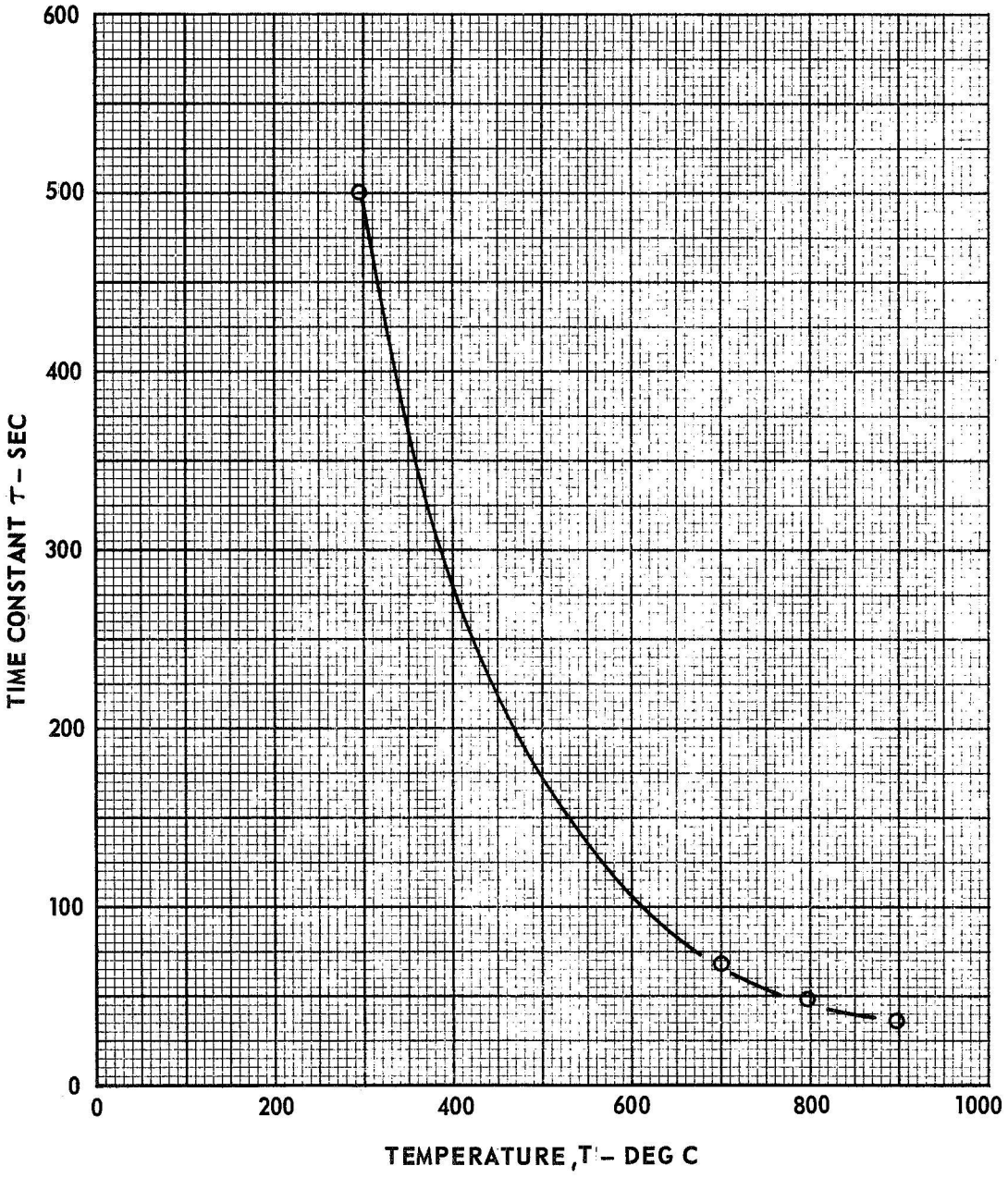

CALCULATED EFFECT OF OPTICAL BLEACHING ON INDUCED ABSORPTION COEFFICIENT

β = RATIO OF INDUCED ABSORPTION COEFFICIENT INCLUDING EFFECT OF OPTICAL BLEACHING TO INDUCED ABSORPTION COEFFICIENT IN THE ABSENCE OF OPTICAL BLEACHING

b = ELECTRON TRAPPING CONSTANT – MRAD^{-1}

τ = THERMAL DECOLORATION TIME CONSTANT – SEC

c = OPTICAL BLEACHING CONSTANT – WATTS^{-1} CM^2 – SEC^{-1}

I = LIGHT INTENSITY – WATTS/CM^2

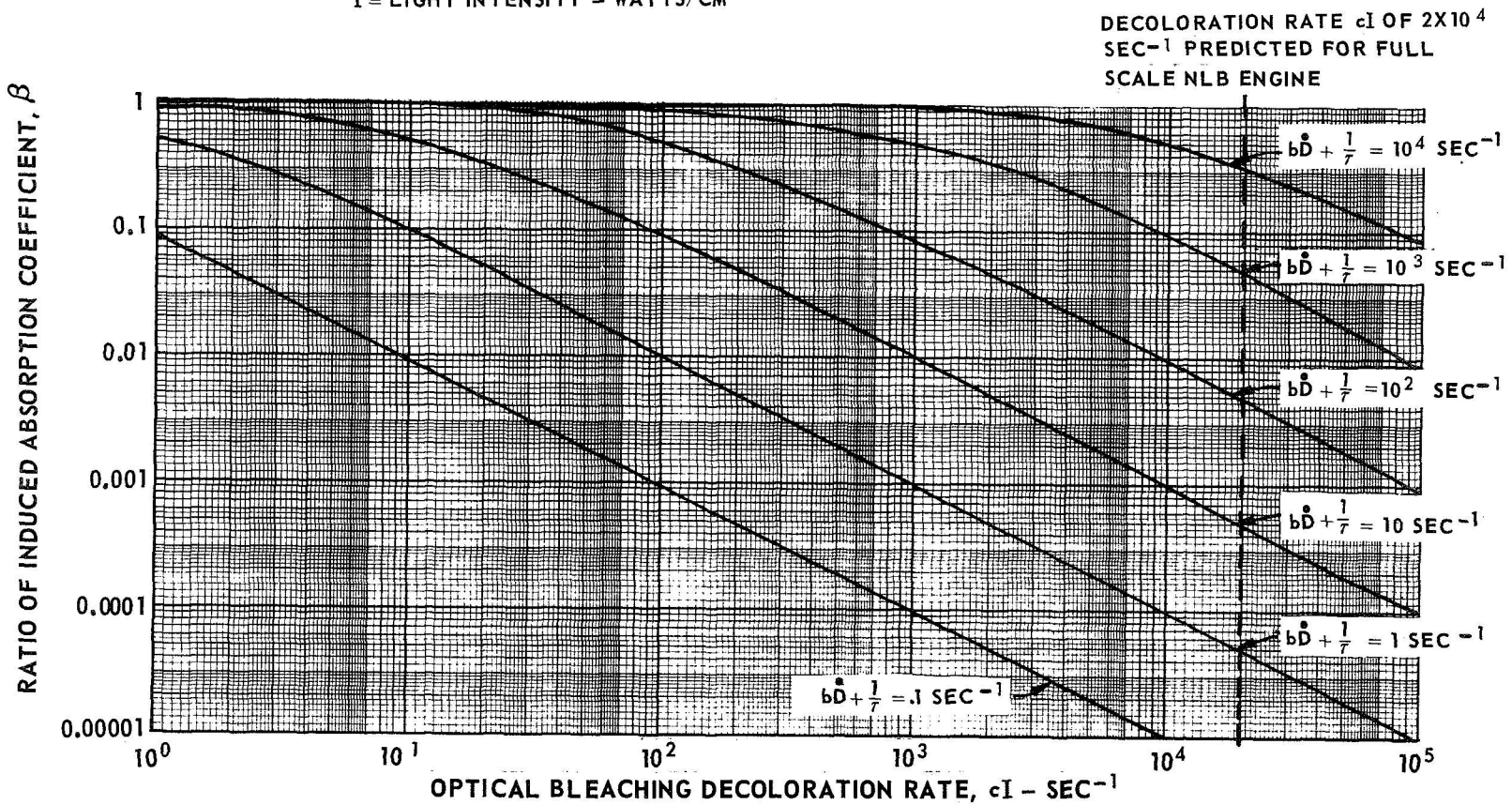

FIG. 4

ELECTRICAL AND OPTICAL SCHEMATIC FOR ELECTRON IRRADIATION EXPERIMENTS

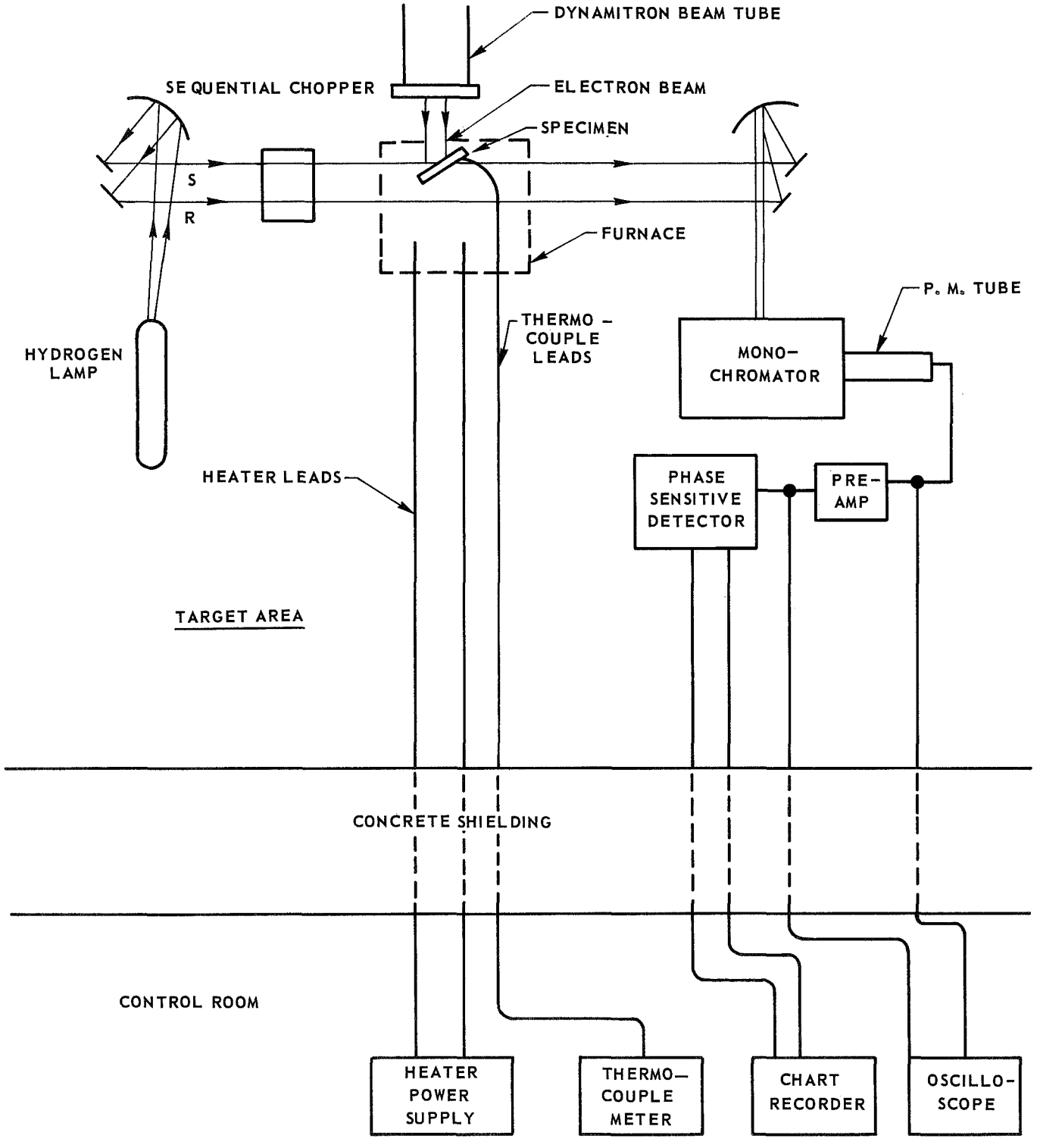

H-930709-1

FIG. 6

ELECTRON CURRENT DENSITY, SPECIMEN TEMPERATURE AND INDUCED ABSORPTION COEFFICIENT DURING RUN 12

λ = 4500 Å SPECIMEN D-3

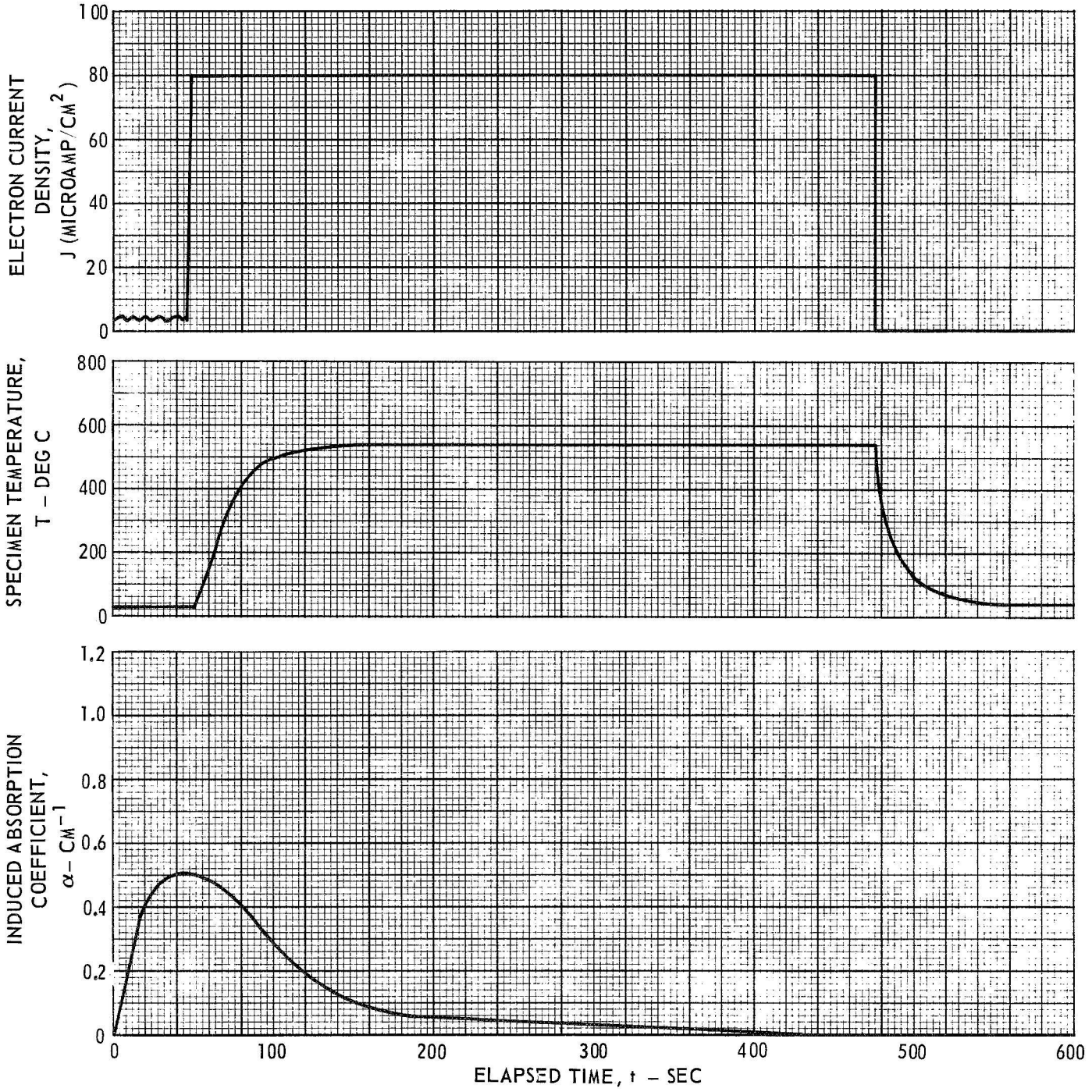

FIG. 7

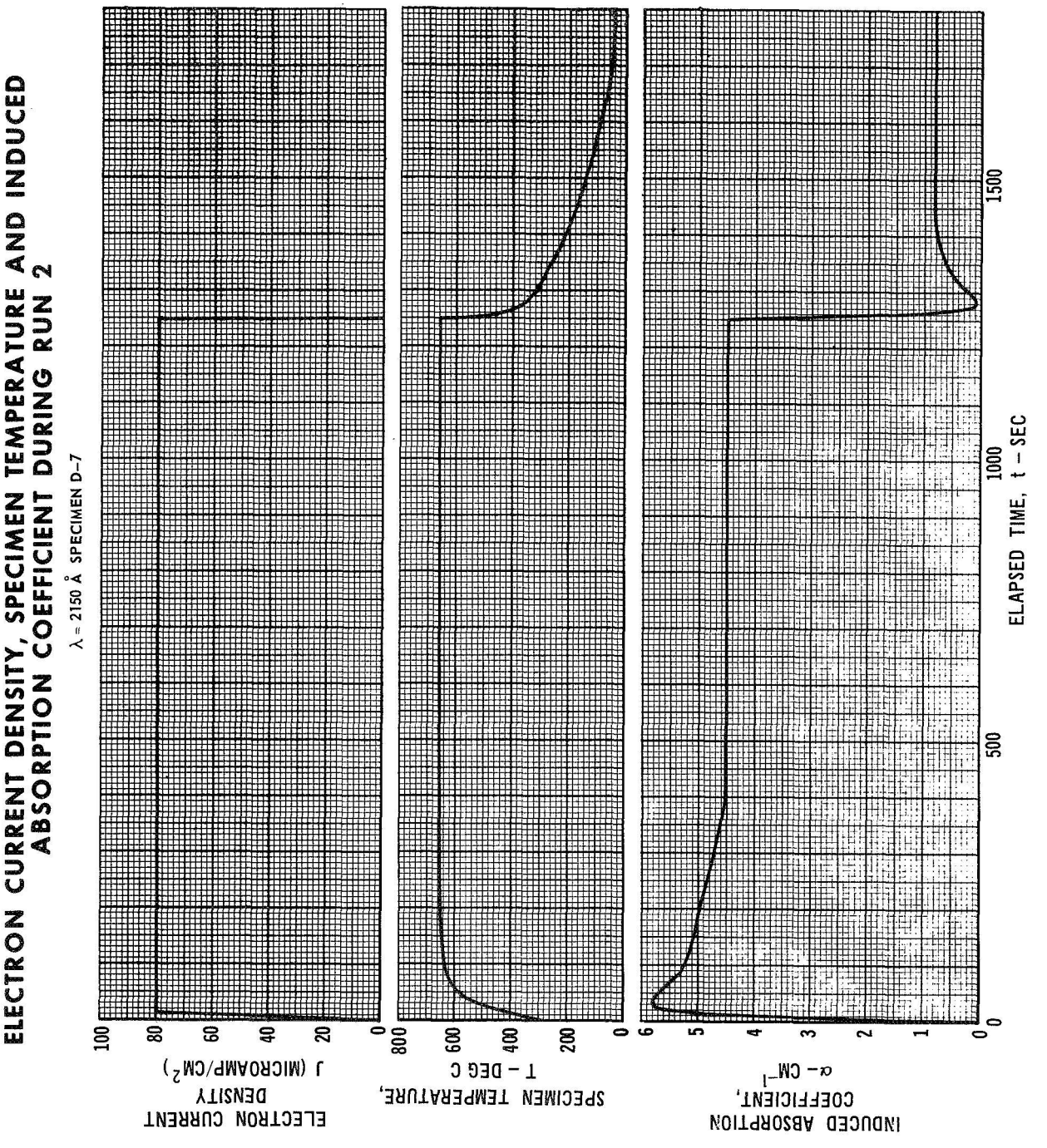
ELECTRON CURRENT DENSITY, SPECIMEN TEMPERATURE AND INDUCED ABSORPTION COEFFICIENT DURING RUN 2
λ = 2150 Å SPECIMEN D–7
ELECTRON CURRENT DENSITY
J (MICROAMP/CM²)
100
80
60
40
20
0
SPECIMEN TEMPERATURE, T – DEG C
800
600
400
200
0
INDUCED ABSORPTION COEFFICIENT, α – CM⁻¹
6
5
4
3
2
1
0
0
500
1000
1500
ELAPSED TIME, t – SEC

ELECTRON CURRENT DENSITY, SPECIMEN TEMPERATURE AND INDUCED ABSORPTION COEFFICIENT DURING RUN 7

λ= 2150 Å SPECIMEN D-5

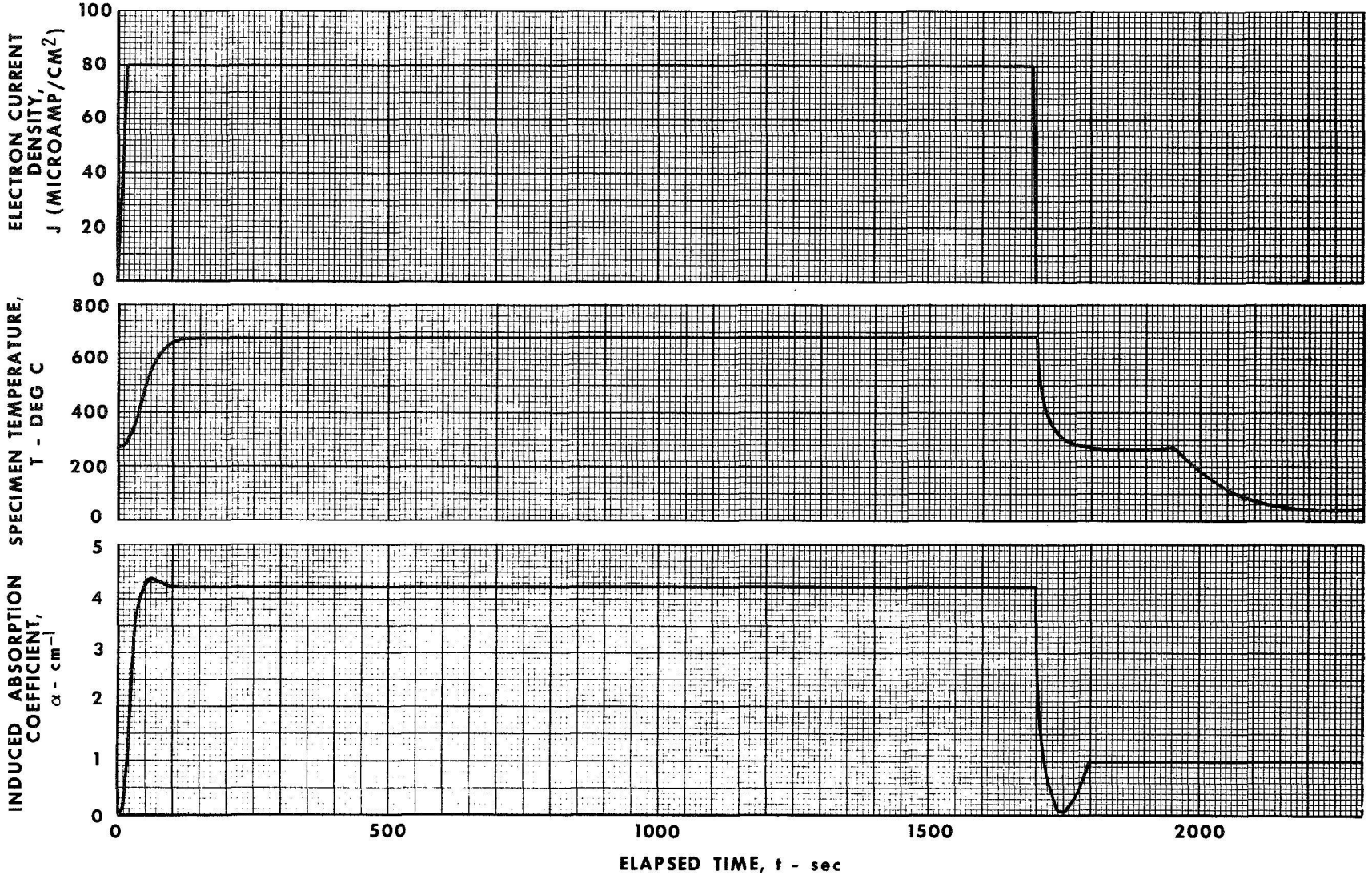

FIG. 8

FIG. 9

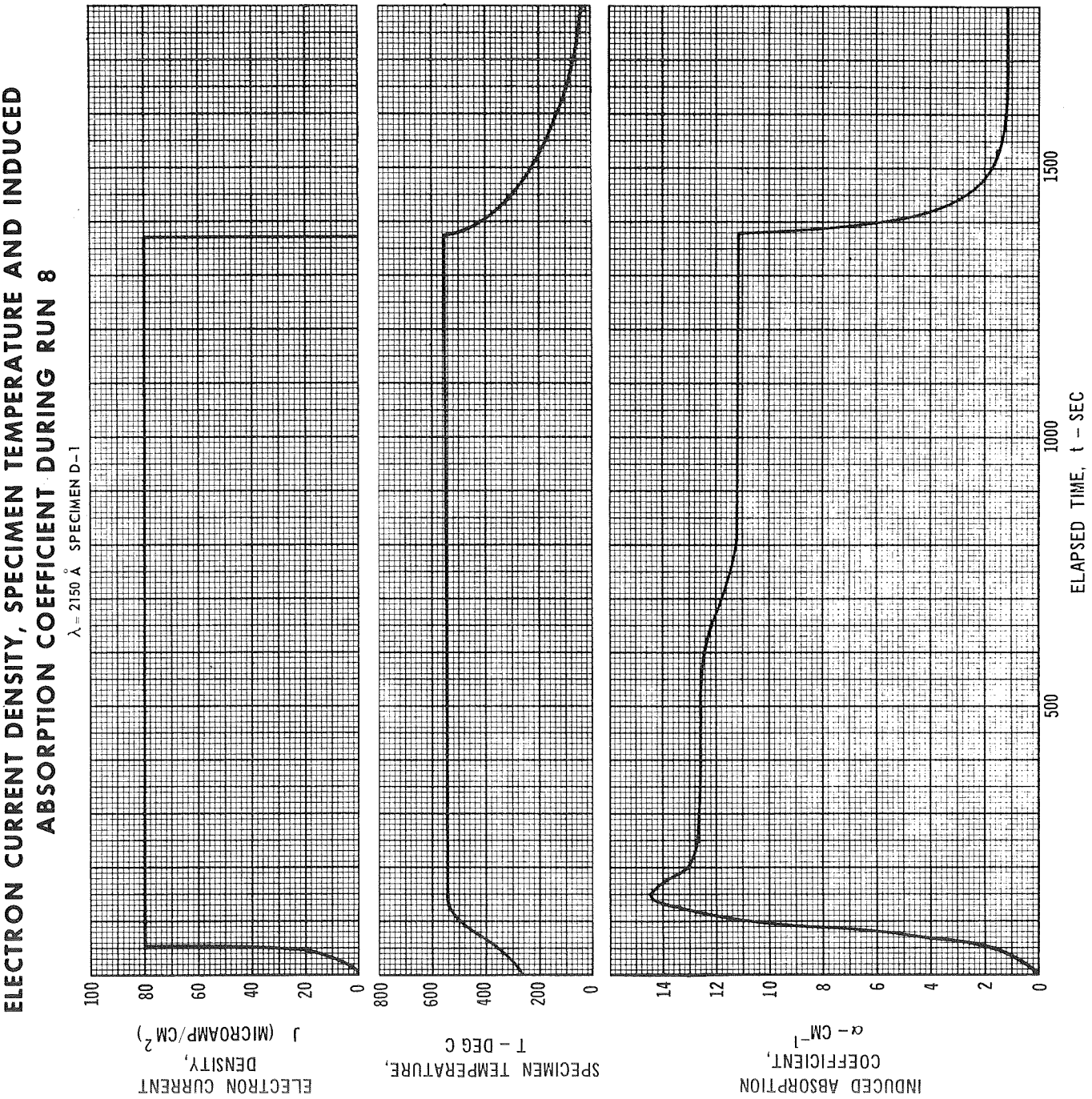
ELECTRON CURRENT DENSITY, SPECIMEN TEMPERATURE AND INDUCED ABSORPTION COEFFICIENT DURING RUN 8
λ = 2150 Å SPECIMEN D-1
ELECTRON CURRENT DENSITY, J (MICROAMP/CM²)
100
80
60
40
20
0
SPECIMEN TEMPERATURE, T - DEG C
800
600
400
200
0
INDUCED ABSORPTION COEFFICIENT, α - CM⁻¹
14
12
10
8
6
4
2
0
500
1000
1500
ELAPSED TIME, t - SEC

FIG. 10

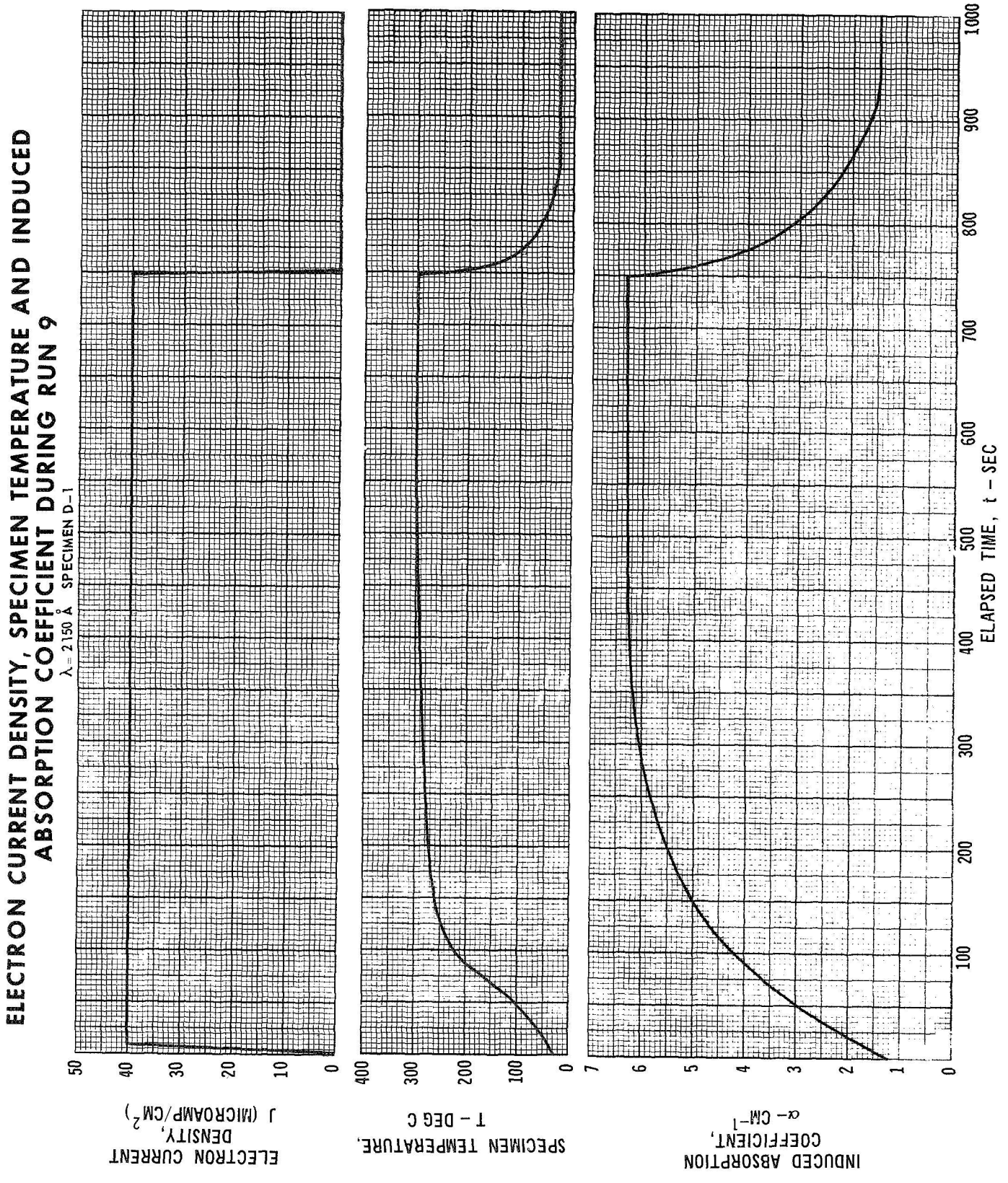
ELECTRON CURRENT DENSITY, SPECIMEN TEMPERATURE AND INDUCED ABSORPTION COEFFICIENT DURING RUN 9
λ = 2150 Å SPECIMEN D-1
ELECTRON CURRENT DENSITY, J (MICROAMP/CM²)
SPECIMEN TEMPERATURE, T - DEG C
INDUCED ABSORPTION COEFFICIENT, α - CM⁻¹
ELAPSED TIME, t - SEC
0
10
20
30
40
50
100
200
300
400
1
2
3
4
5
6
7
100
200
300
400
500
600
700
800
900
1000

ELECTRON CURRENT DENSITY, SPECIMEN TEMPERATURE AND INDUCED ABSORPTION COEFFICIENT DURING RUN 10

λ = 2150 Å SPECIMEN D-1

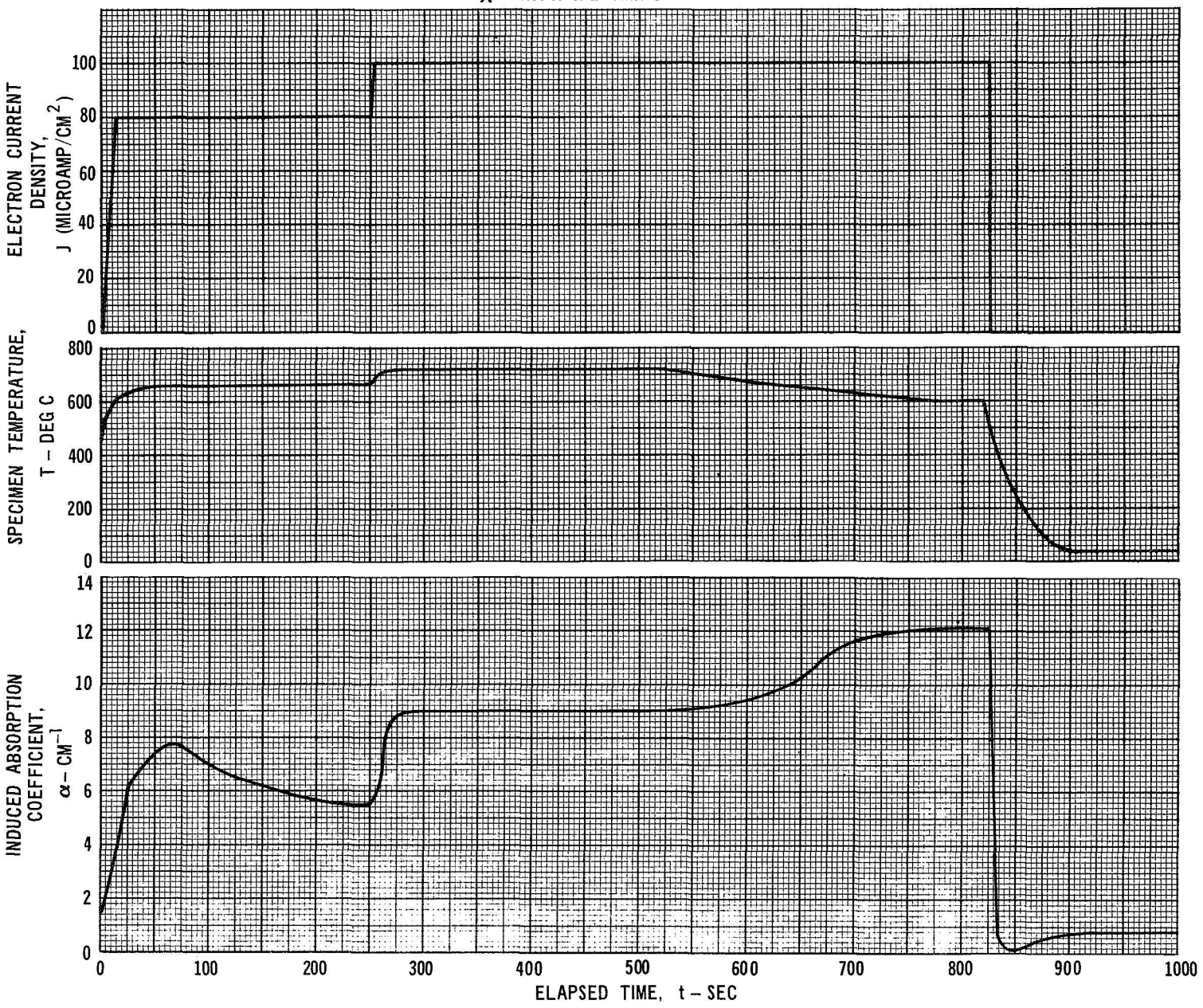

FIG. 11

FIG. 12

ELECTRON CURRENT DENSITY, SPECIMEN TEMPERATURE AND INDUCED ABSORPTION COEFFICIENT DURING RUN 13

λ = 2150 Å SPECIMEN D-2

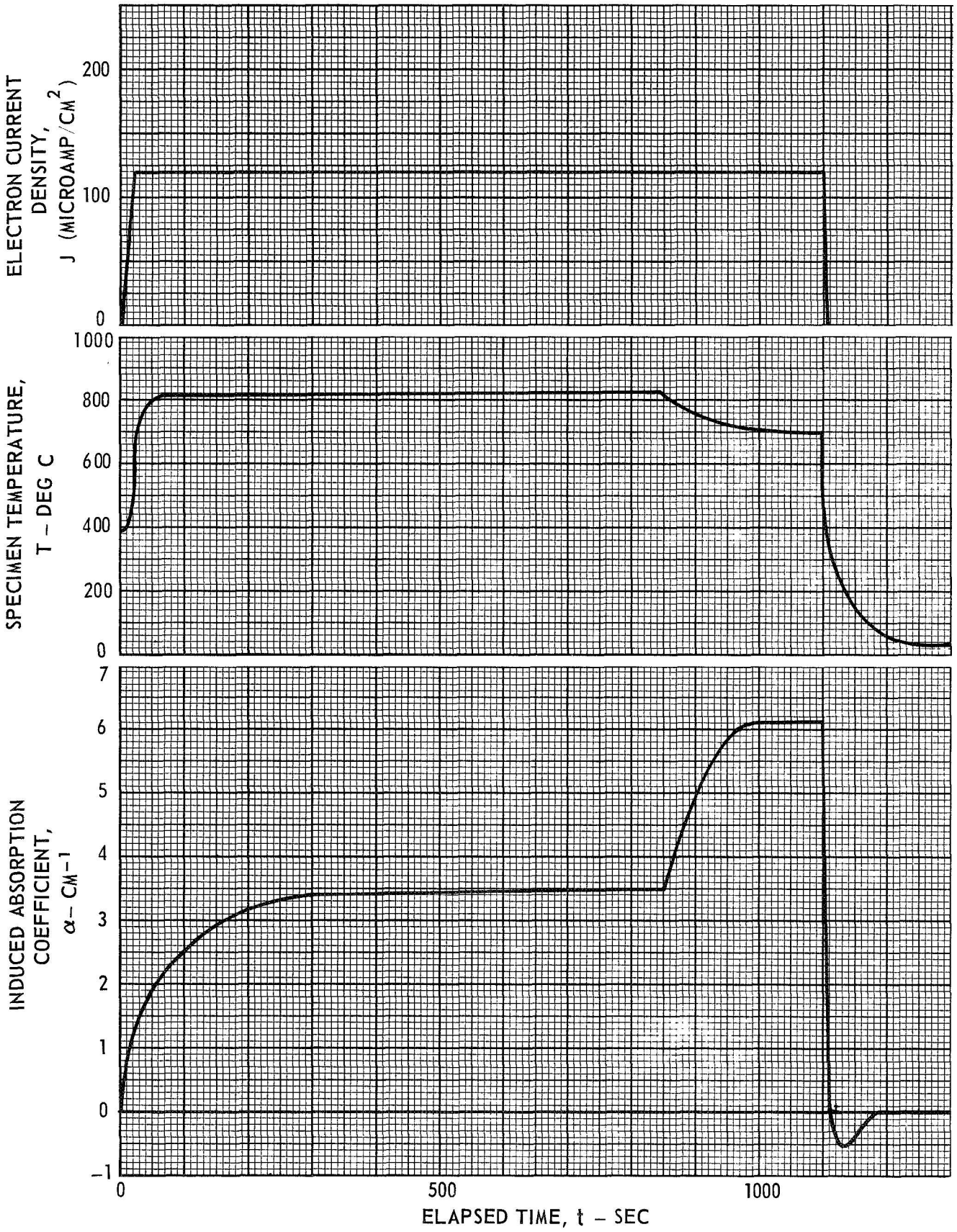

ELECTRON CURRENT DENSITY, SPECIMEN TEMPERATURE AND INDUCED ABSORPTION COEFFICIENT DURING RUN 14

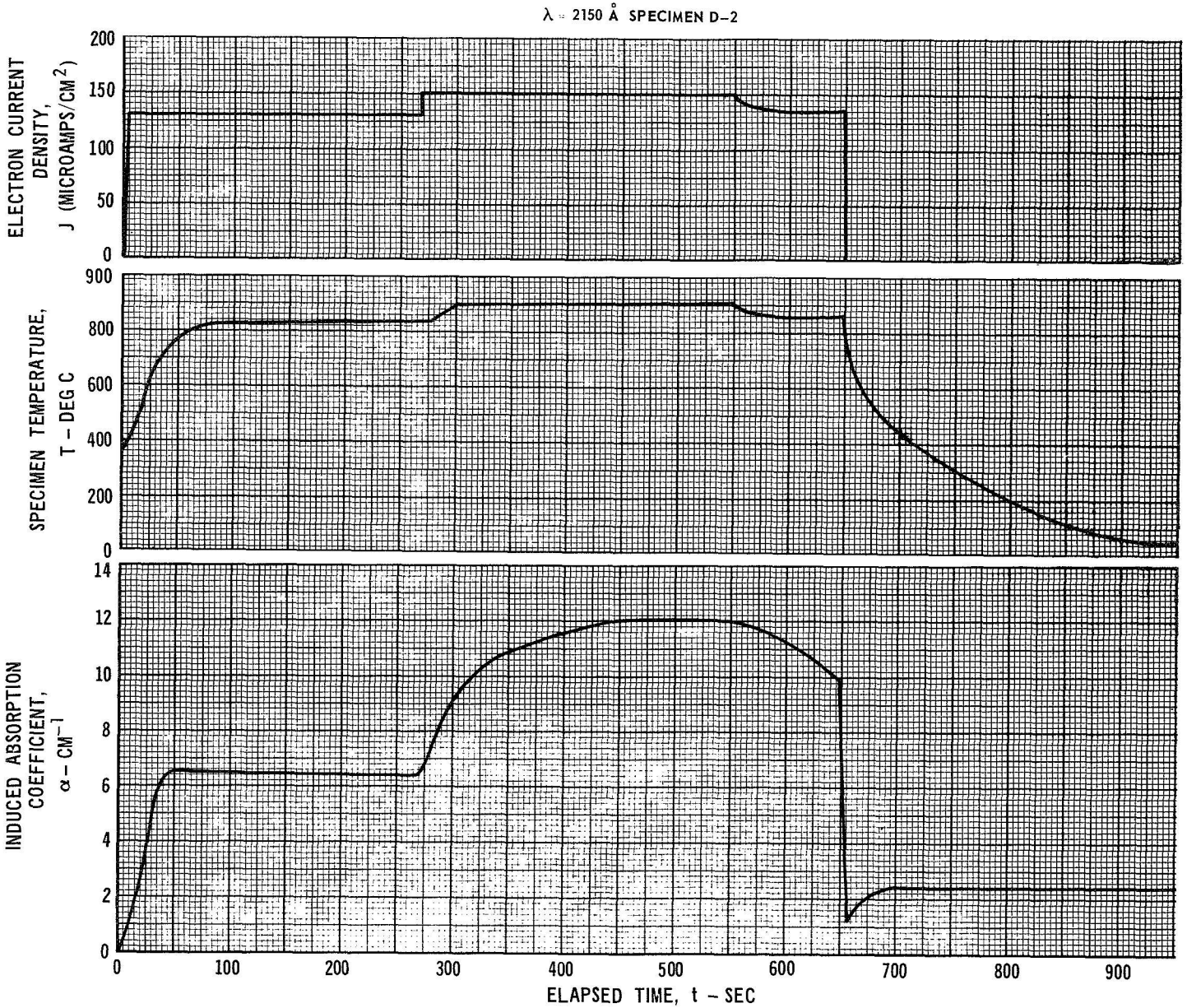

FIG. 13

FIG. 14

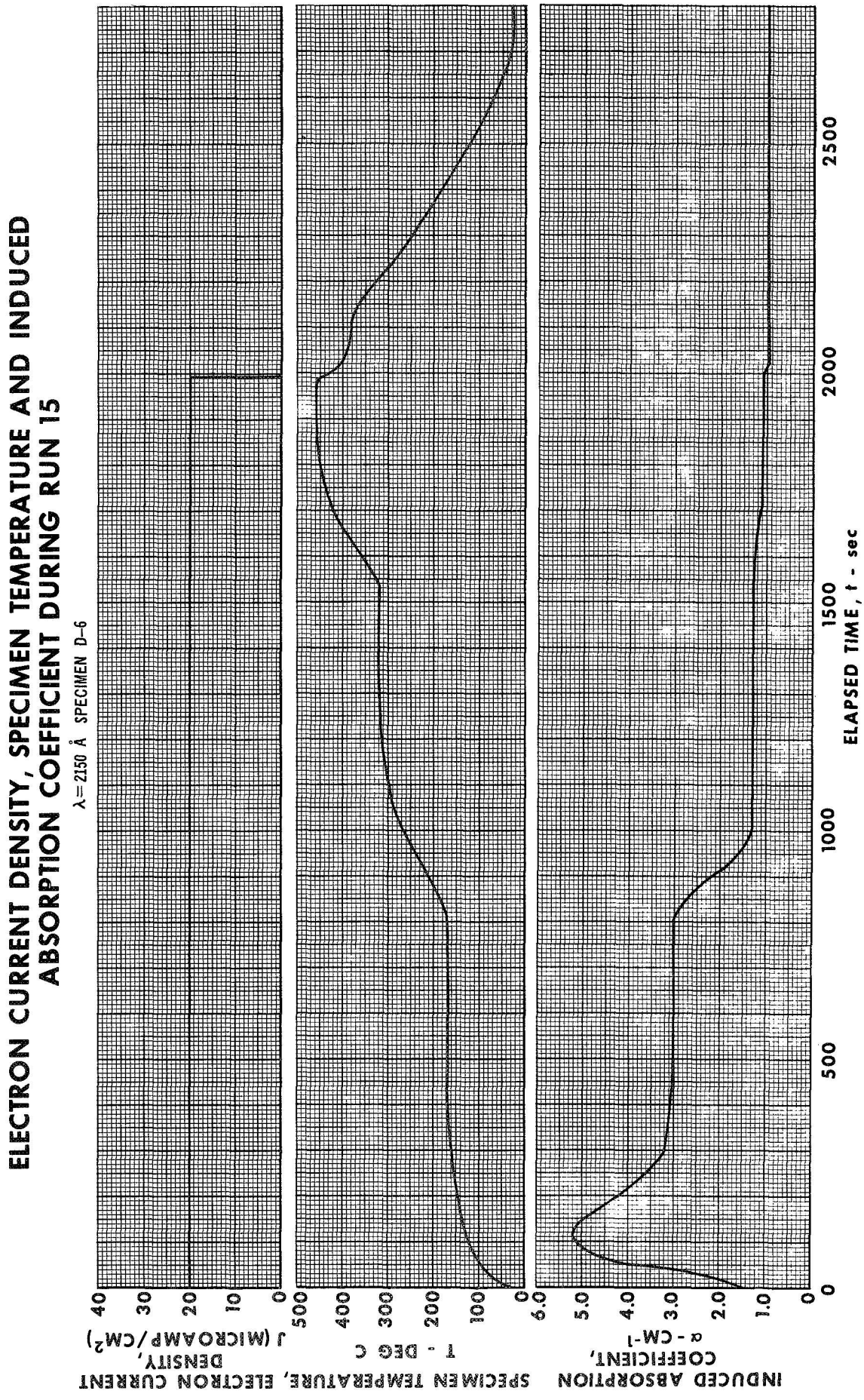
ELECTRON CURRENT DENSITY, SPECIMEN TEMPERATURE AND INDUCED ABSORPTION COEFFICIENT DURING RUN 15
λ = 2150 Å SPECIMEN D-6
INDUCED ABSORPTION COEFFICIENT, α - CM-1
SPECIMEN TEMPERATURE, T - DEG C
ELECTRON CURRENT DENSITY, J (MICROAMP/CM2)
ELAPSED TIME, t - sec
0
1.0
2.0
3.0
4.0
5.0
6.0
100
200
300
400
500
10
20
30
40
500
1000
1500
2000
2500

ELECTRON CURRENT DENSITY, SPECIMEN TEMPERATURE AND INDUCED ABSORPTION COEFFICIENT DURING RUN 16

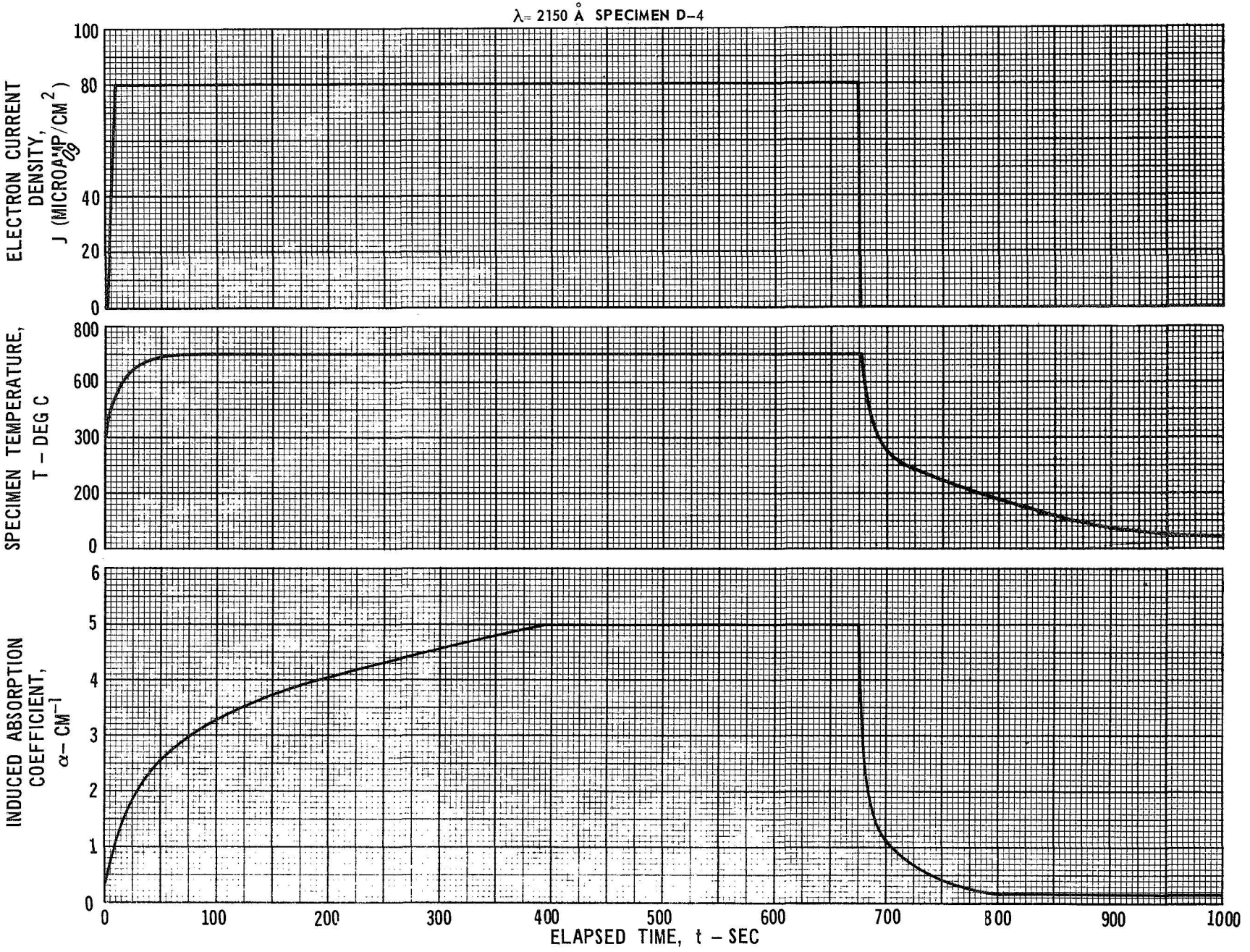

FIG. 15

NORMALIZED SOLUTION OF KINETIC EQUATIONS FOR DEFECT GENERATION BY IONIZING RADIATION

$b\dot{D}$ = ELECTRON TRAPPING RATE = 10^4 SEC^{-1}

τ_B = THERMAL BLEACHING TIME CONSTANT = 1 SEC

τ_A = THERMAL ANNEALING TIME CONSTANT = 100 SEC

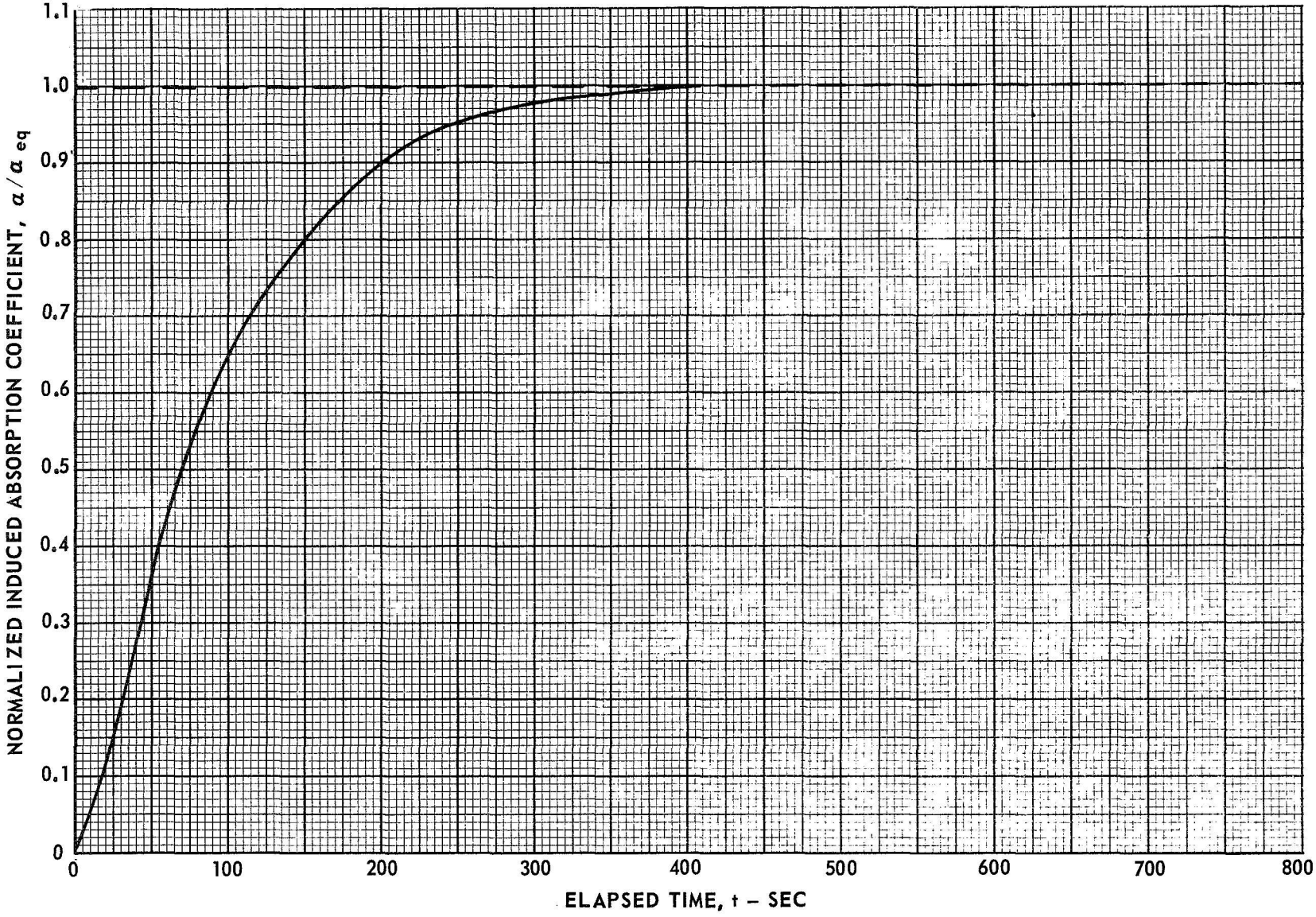

FIG. 16

NORMALIZED SOLUTIONS OF KINETIC EQUATIONS FOR FIXED CONCENTRATION OF DEFECTS

$b\mathring{D}$ = ELECTRON TRAPPING RATE = 10^{-2} SEC^{-1}

τ_B = THERMAL BLEACHING TIME CONSTANT = 10 SEC

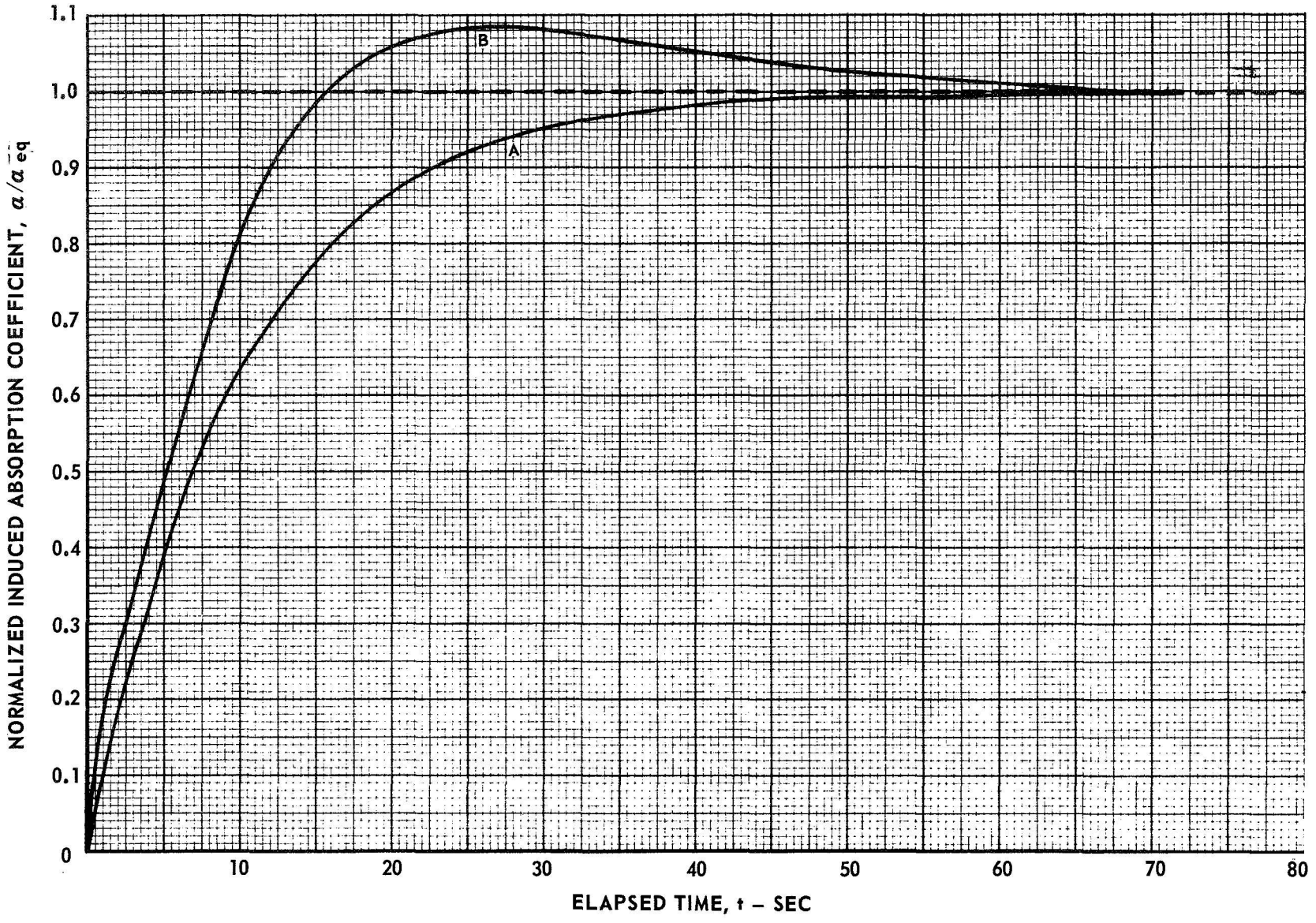

FIG. 17

FIG. 18

EQUILIBRIUM INDUCED ABSORPTION COEFFICIENT AT ELEVATED SPECIMEN TEMPERATURES DURING ELECTRON IRRADIATIONS

$\lambda = 2150$ Å

SYMBOL	MICROAMP/CM^2	R/SEC
▲	150	$2X10^7$
●	130	$1.74X10^7$
■	120	$1.6X10^7$
△	100	$1.34X10^7$
○	80	$1.06X10^7$
□	40	$5.35X10^6$
▽	20	$2.67X10^6$

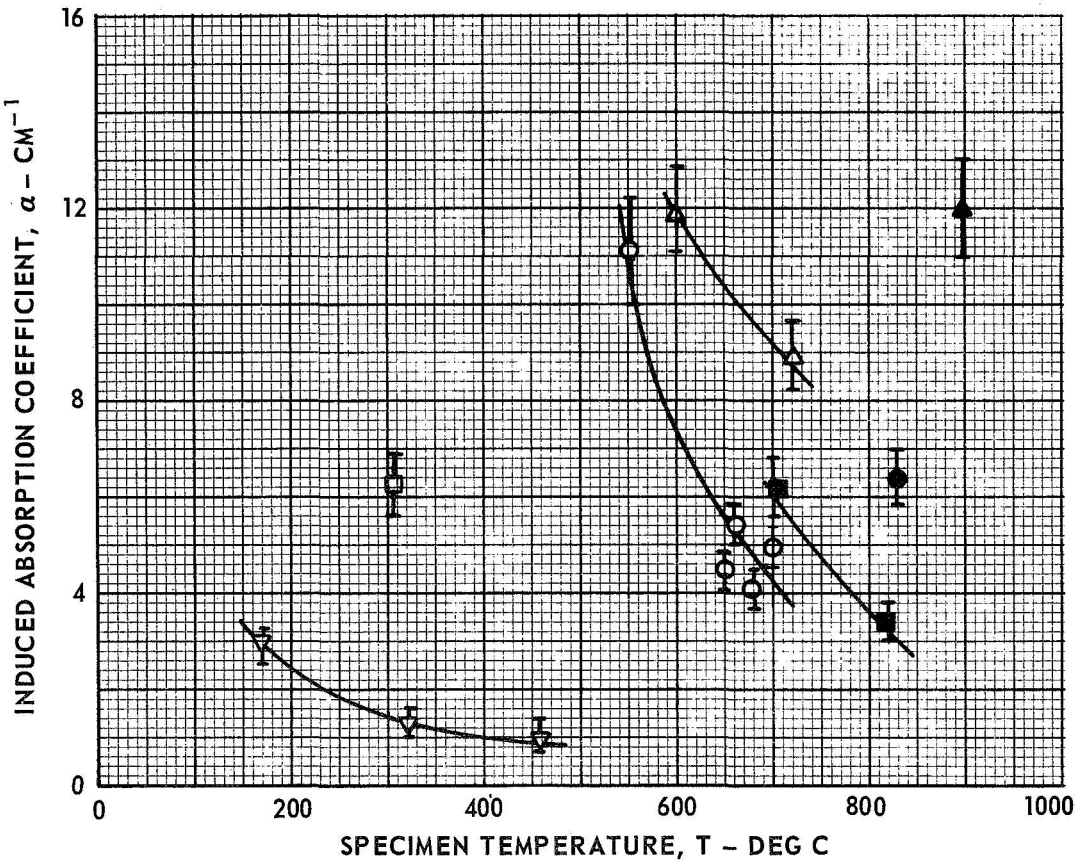

COMPARISON OF NEUTRON ENERGY SPECTRUMS FOR REACTOR EXPERIMENT AND FOR FULL SCALE NLB-ENGINE

(FOR NEUTRON ENERGIES E > 0.75 MEV)

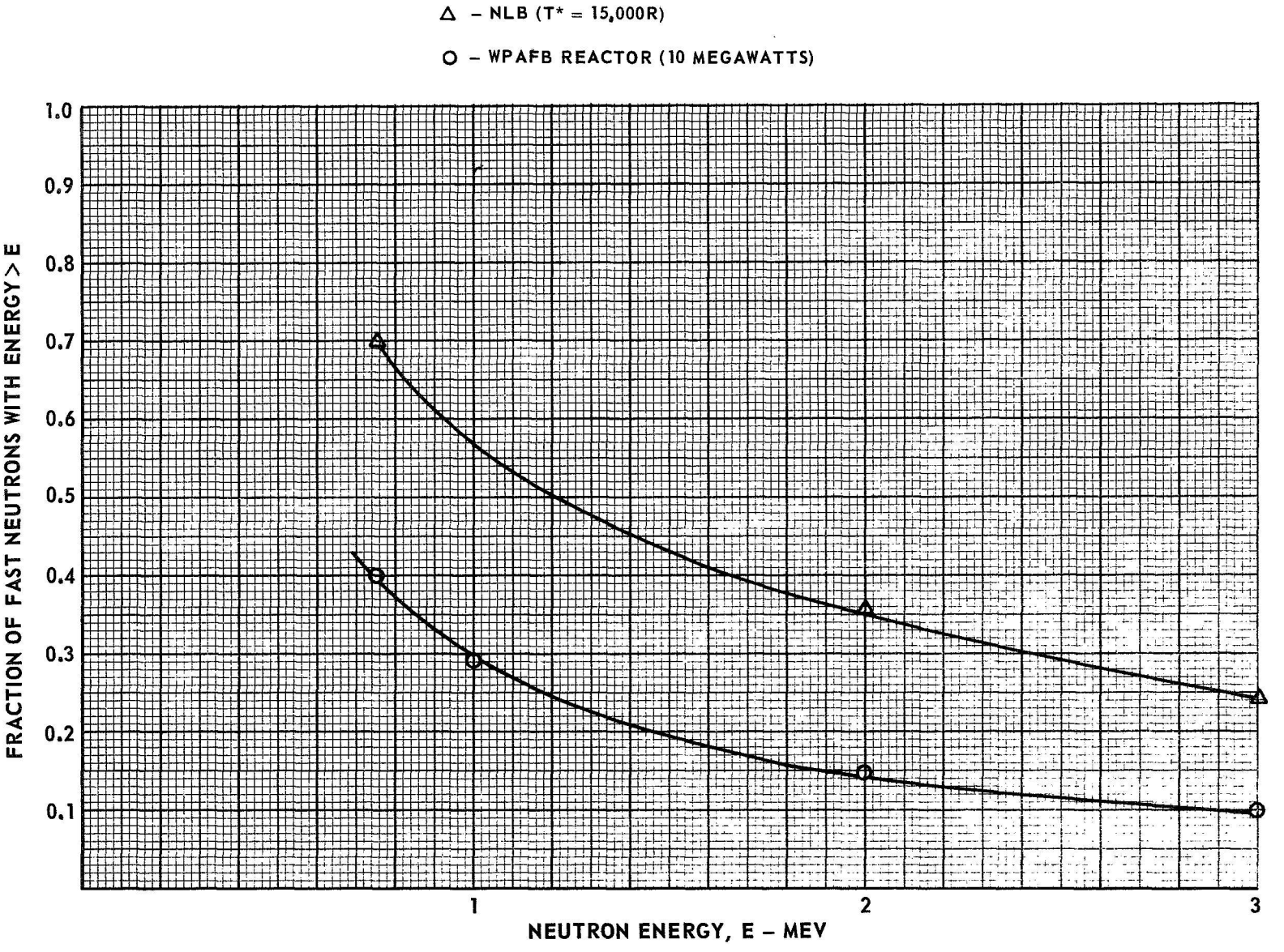

FIG. 19

ELECTRICAL AND OPTICAL SCHEMATIC FOR WPAFB NUCLEAR REACTOR EXPERIMENTS

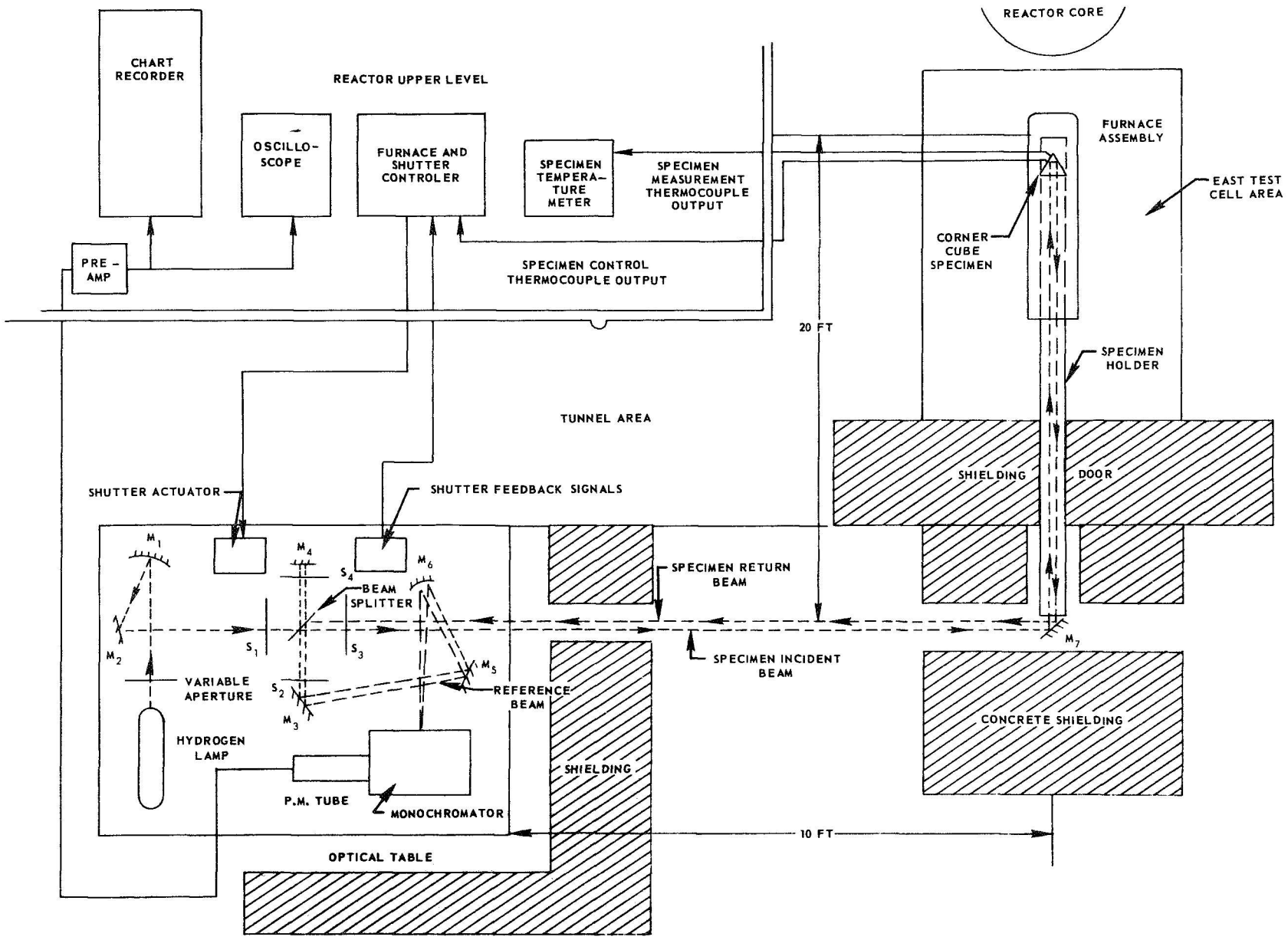

H-930709-1

FIG. 20

IONIZING DOSE RATE VS DISTANCE FROM REACTOR CORE FACE AT REACTOR POWER OF 10 MEGAWATTS

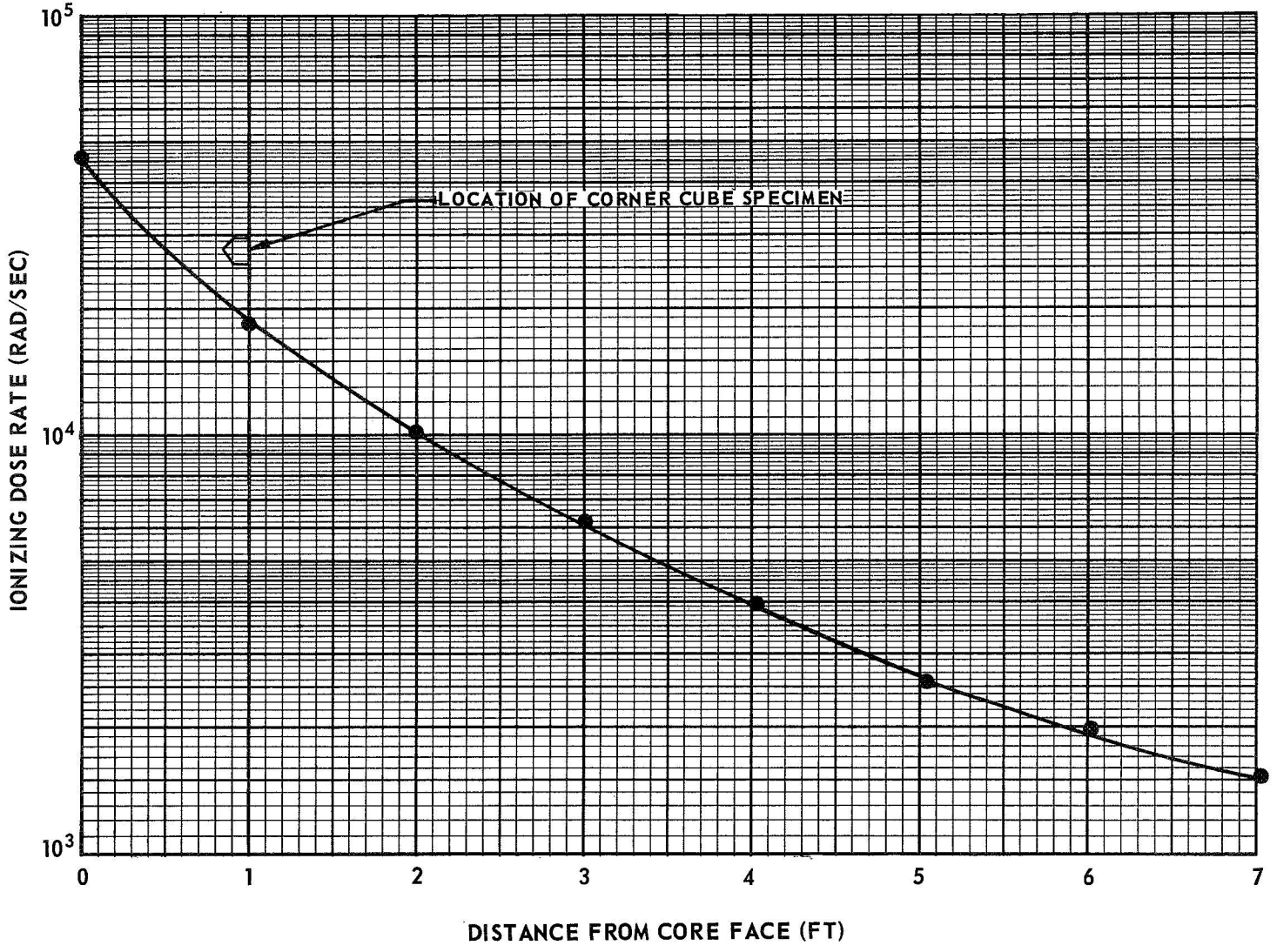

FIG. 21

REACTOR IRRADIATION AND TEMPERATURE HISTORY FOR SPECIMEN R-1

TOTAL IONIZING DOSE = 8.1×10^9 R

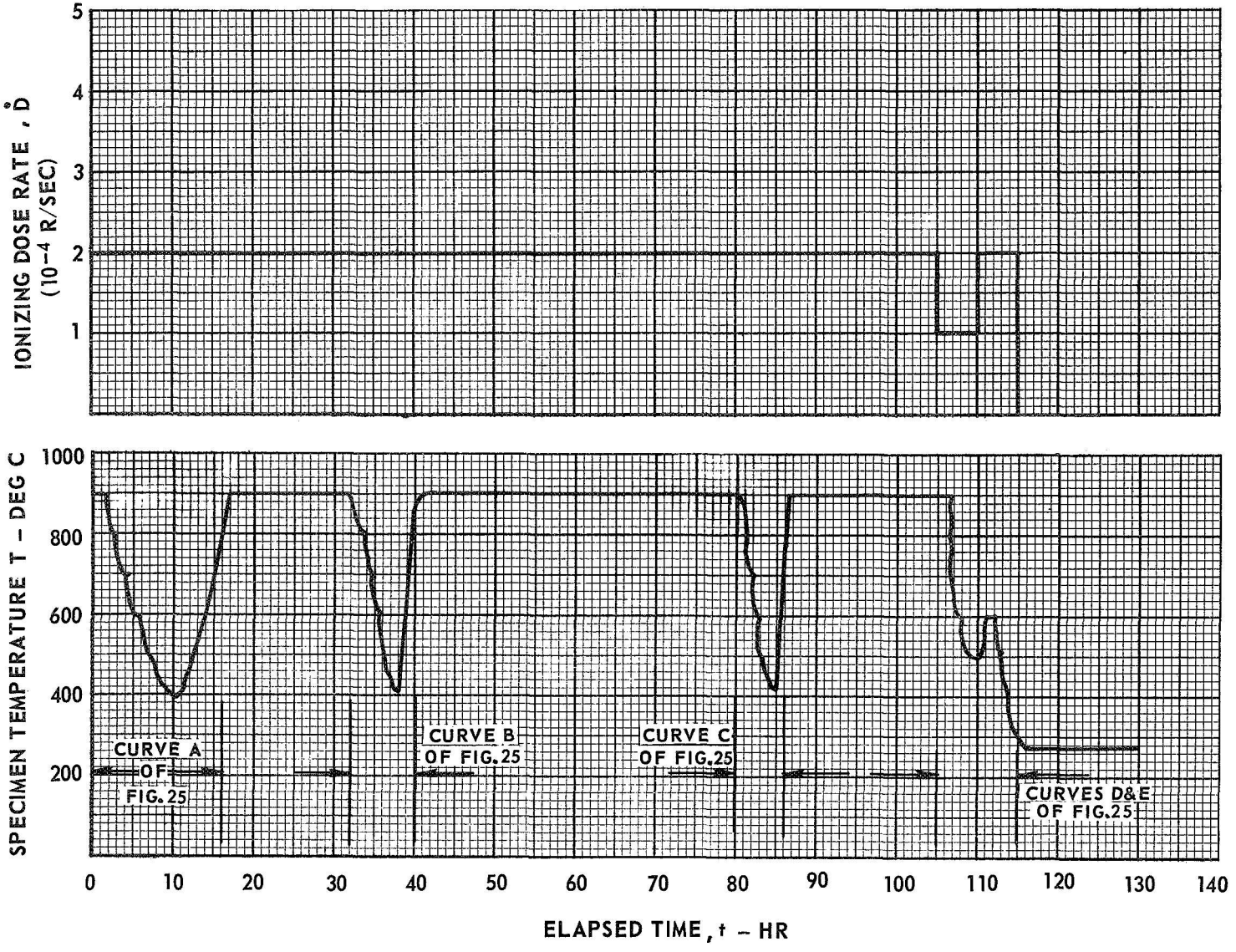

FIG. 22

REACTOR IRRADIATION AND TEMPERATURE HISTORY FOR SPECIMEN R-2

TOTAL IONIZING DOSE = 7.6×10^9 R

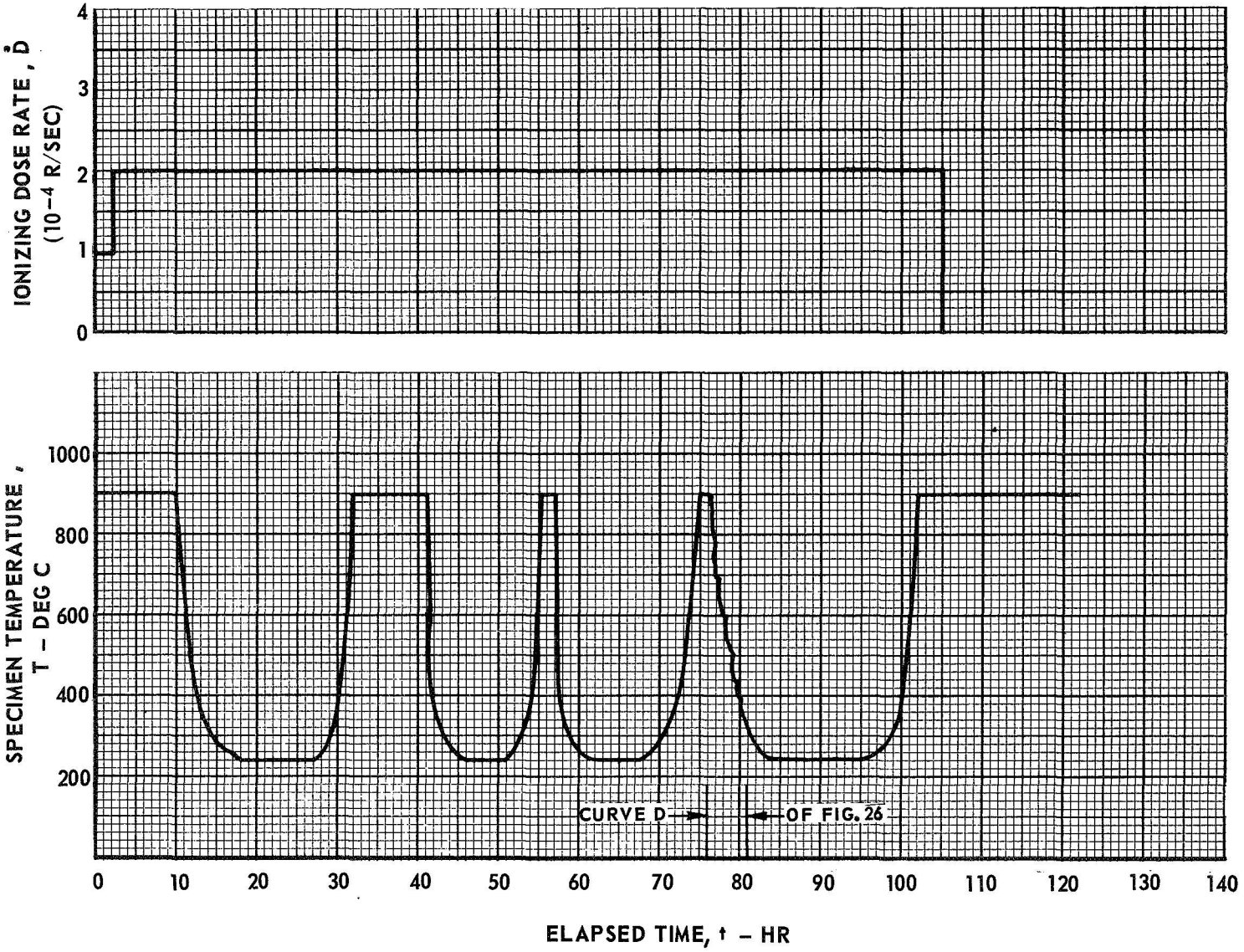

H-930709-1

FIG. 23

REACTOR IRRADIATION AND TEMPERATURE HISTORY FOR SPECIMEN R-3

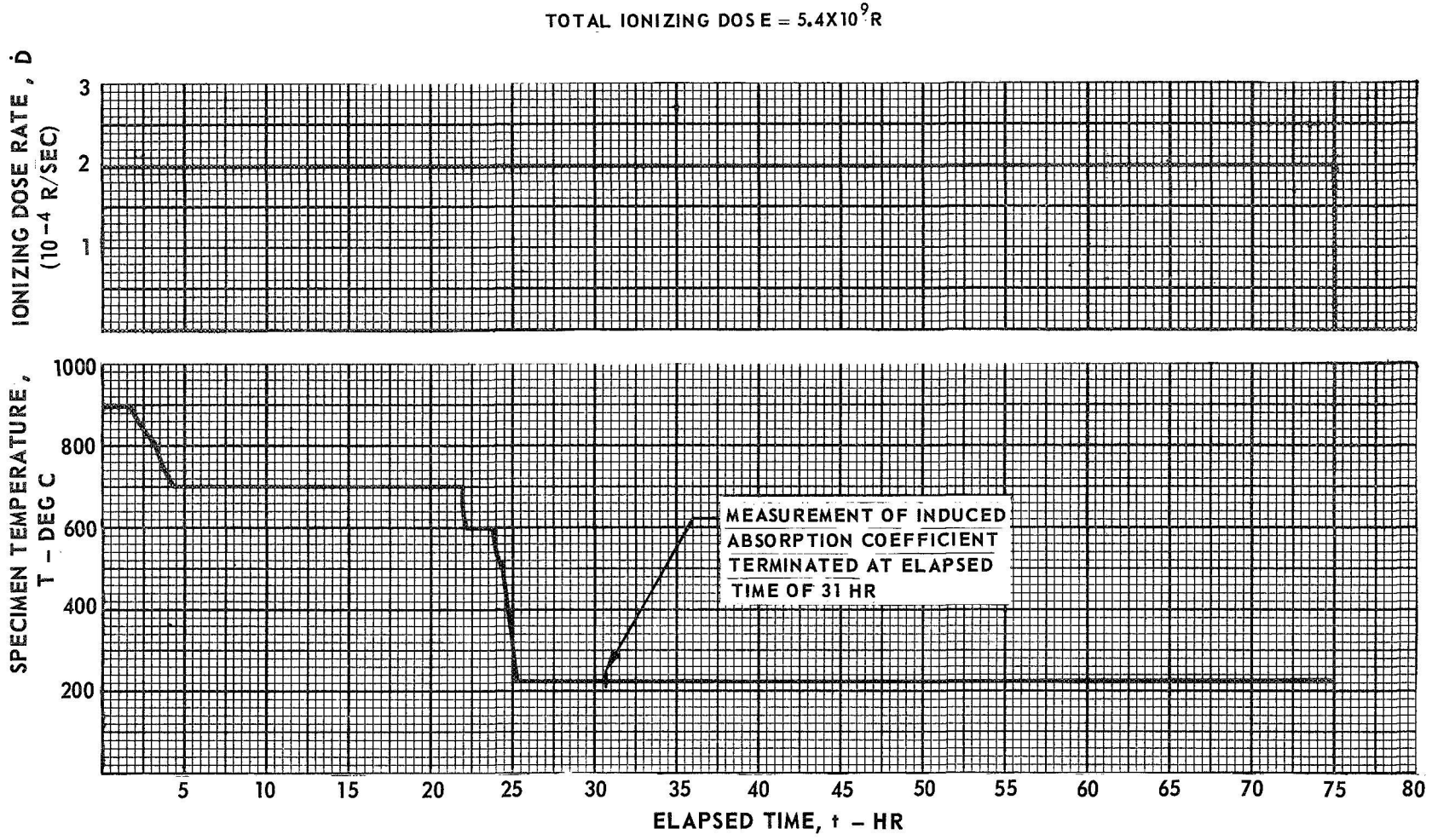

FIG. 24

FIG. 25

EQUILIBRIUM INDUCED ABSORPTION COEFFICIENT VS SPECIMEN TEMPERATURE DURING REACTOR IRRADIATION FOR SPECIMEN R-1

$\lambda = 2150$ Å

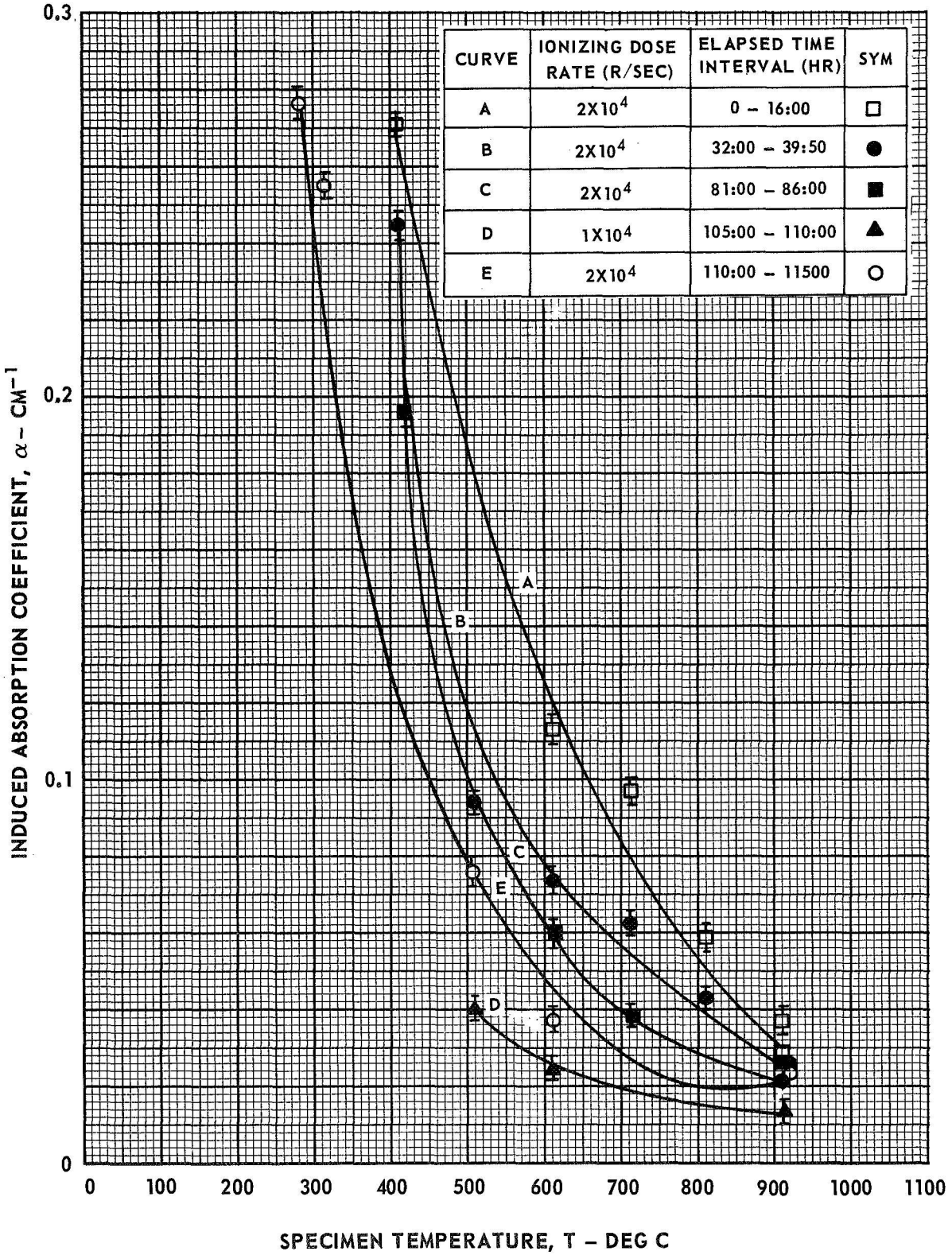

EQUILIBRIUM INDUCED ABSORPTION COEFFICIENT VS SPECIMEN TEMPERATURE DURING REACTOR IRRADIATION SPECIMEN R-2

$\lambda = 2150$ Å

CURVE	IONIZING DOSE RATE (R/SEC)	ELAPSED TIME INTERVAL	SYM
A	$1X10^4$	0 – 2:50	▲
B	$2X10^4$	2:50 – 11:00	△
C	$2X10^4$	55:00 – 56:30	□
D	$2X10^4$	76:00 – 81:00	○
E	$2X10^4$	106:00	●

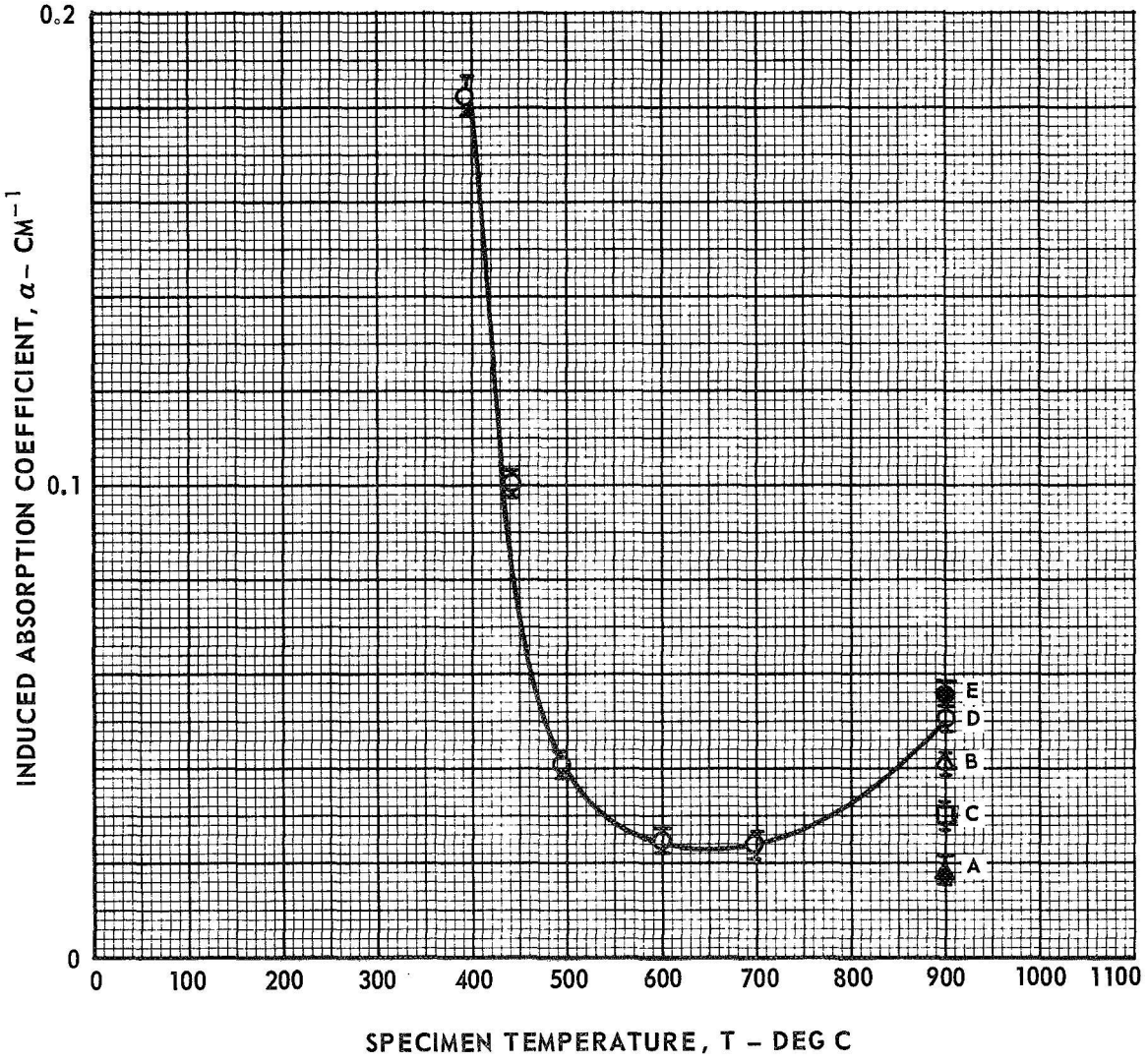

FIG. 27

EQUILIBRIUM INDUCED ABSORPTION COEFFICIENT VS SPECIMEN TEMPERATURE DURING REACTOR IRRADIATION SPECIMEN R-3

$\lambda = 2700$ Å

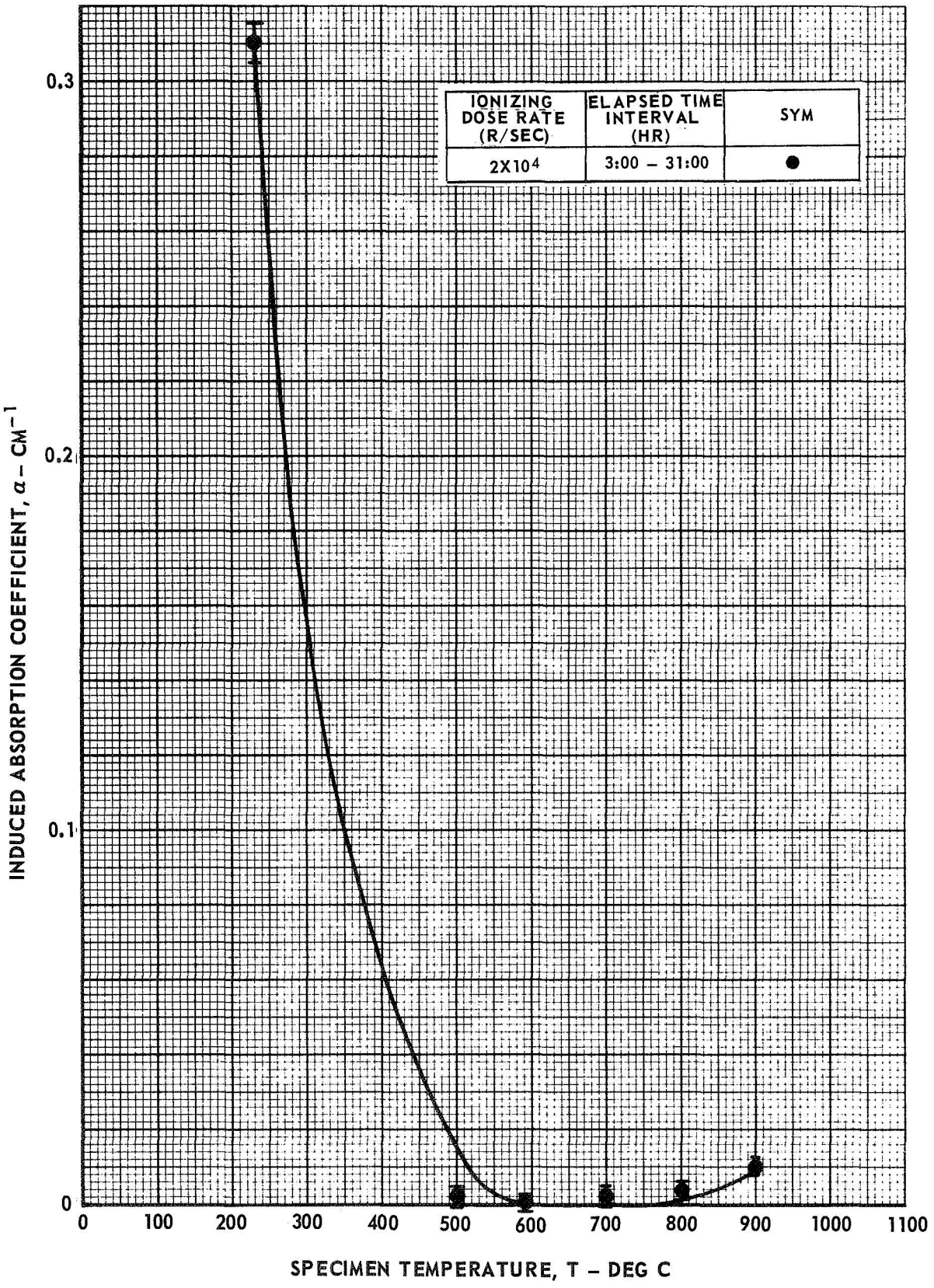

COMPARISON OF EXPERIMENTAL AND CALCULATED ABSORPTION COEFFICIENTS

λ= 2150 Å

SYMBOL	TEMP.
○	700° C
●	800 °C
▲	900 °C

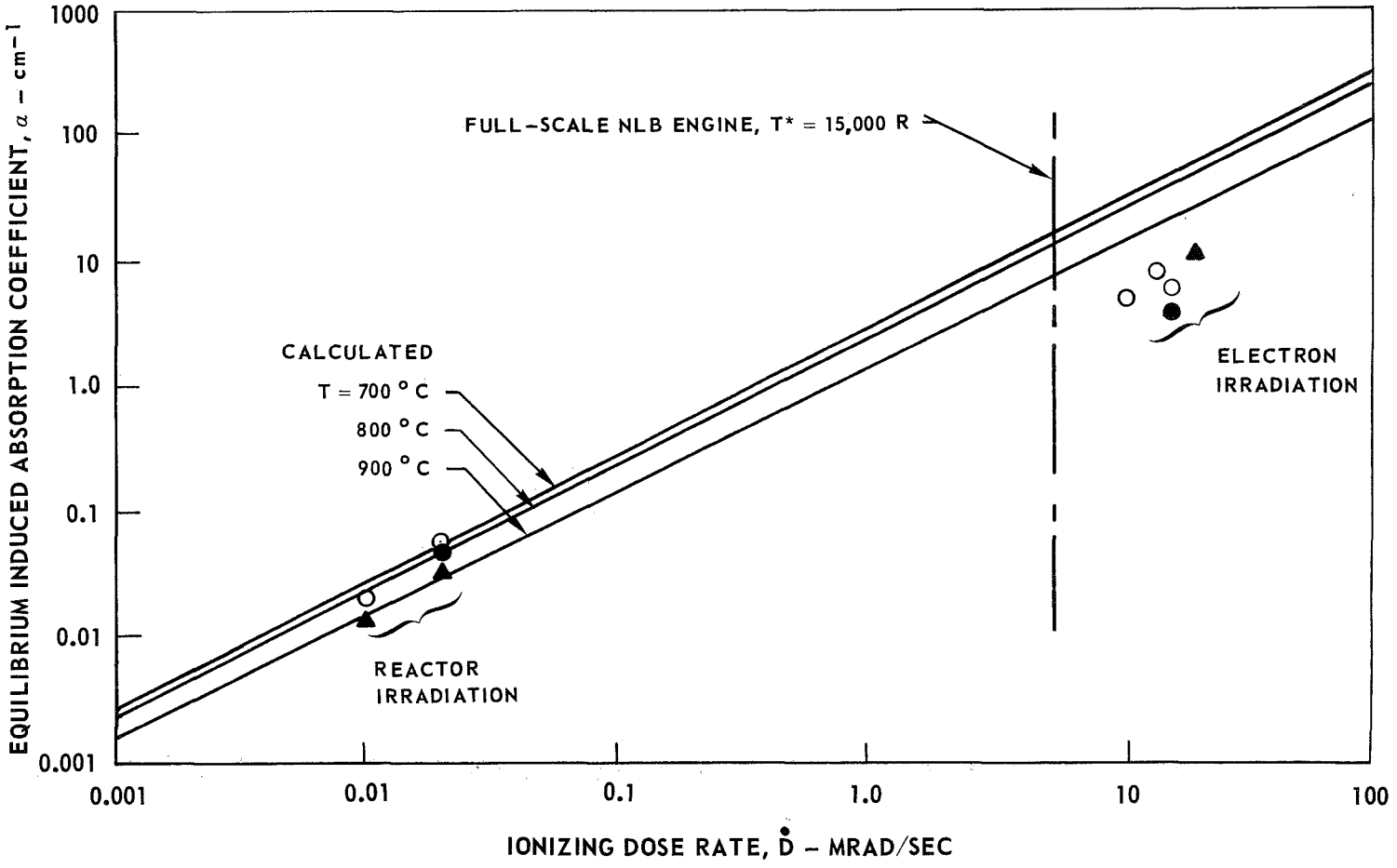

FIG. 28

FRACTIONS OF THE INCIDENT ELECTRON ENERGY ABSORBED AND NUMBER OF ELECTRONS STOPPED IN SPECIMEN

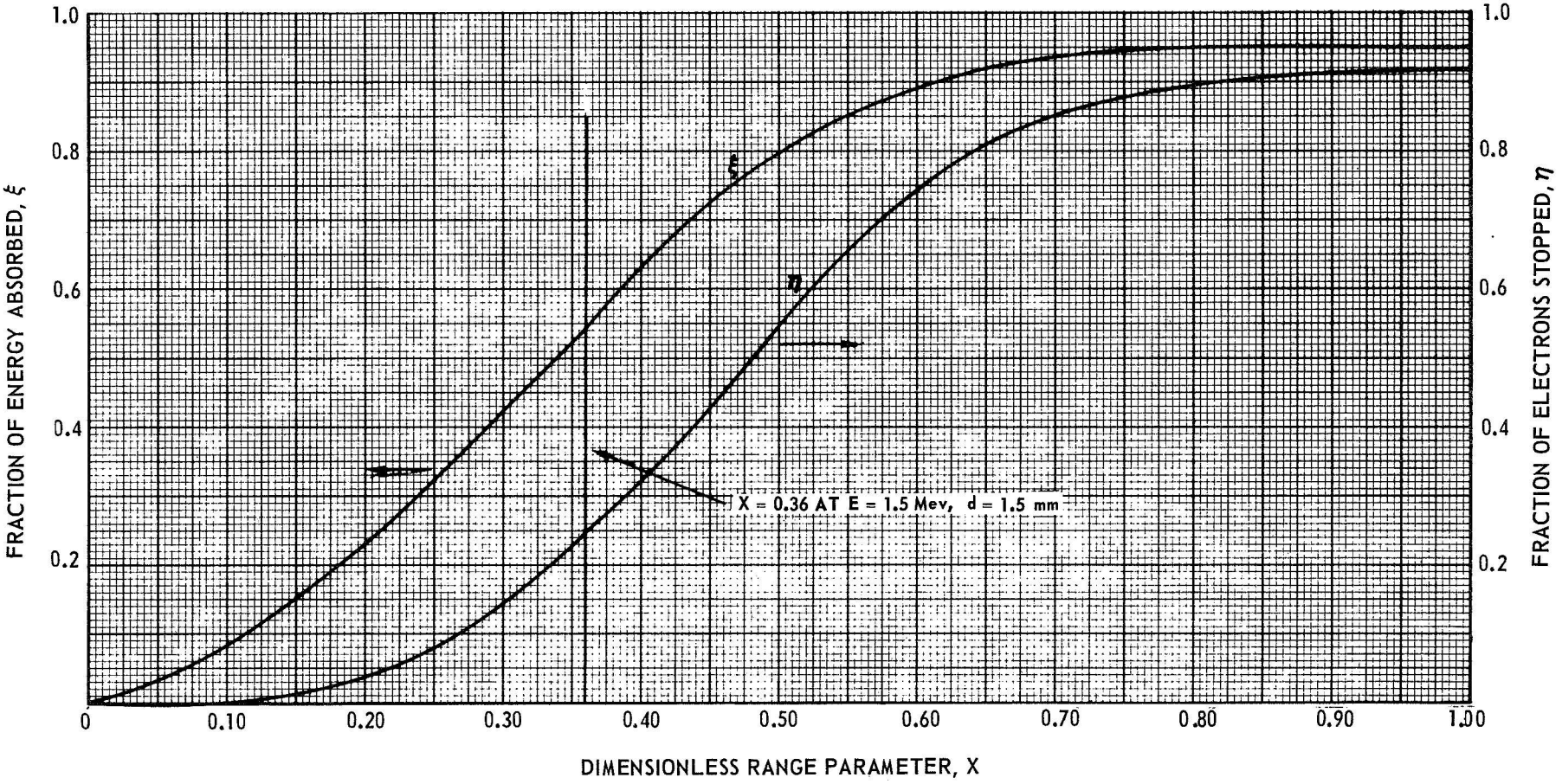

FIG. 29


UNITED AIRCRAFT CORPORATION